Electrochemical Processes Mediated via Adsorbed Enzymes: Flat and Porous Electrodes Compared. Understanding Nano-confinement.

Haonan Le, and Richard G. Compton*

Department of Chemistry, Physical and Theoretical Chemistry Laboratory, Oxford University, South Parks Road, Oxford, OX1 3QZ, United Kingdom.

Abstract

We present theory for electrolysis at electrode surfaces modified by a layer of electroactive enzyme which can mediate the reduction of a substrate to a product. In particular, we compare and contrast immobilisation on flat surfaces with that on porous surfaces. We identify the conditions under which the adoption of porous electrodes facilitates markedly improves turnover rates and develop the analysis on the basis of the porous layer conferring a much-increased *effective* surface coverage. For both types of electrode, the role of the electrode potential in controlling the thermodynamics of the binding of the substrate with the reduced layer of immobilised enzymes is quantified and the observation of apparent potential dependent Michaelis constants explained. Four distinct classes of voltammetric responses are categorised allowing bottom-up process optimisation.

Keywords: Catalysis, enzyme-mediated electrolysis, adsorbed enzyme, simulation, nanoconfinement, nanopores

1 Introduction

Immobilisation offers to improve the performance of enzyme-based catalytic systems notably in terms of stability, efficiency and selectivity [1,2] as a result of the enzyme species being attached to a solid supporting material, where the catalytic reaction takes place. The two most important improvements the immobilisation bring to the overall catalytic performance are, first, the nature of the catalytic processes of the immobilised enzyme shifts from homogeneous to heterogeneous, leading to a better separation of the enzyme and the product, potentially increasing the reusability of the enzyme system and possibly leading to a higher purity product [3]. Second, the enzyme is attached to the supporting surface, which can make the catalytic system more durable allowing more repeated use and application for long periods [1]. Immobilising enzymes in nano-scale structures, so-called nano-confinement, has been realised in diverse structures including nanopores [4-7], nanochannels [8-11], etc, to take advantage of the large reaction area to volume ratios offered at the nanoscale.

Whilst immobilised enzymes have been rigorously investigated in fundamental electrochemical studies [7, 12-18] the application to electro-synthesis of using immobilised enzymes to mediate electron transfer may offer new possibilities in electrosynthesis combining the advantages of heterogeneous catalysis with the selectivity of enzyme chemistry and the intrinsically green nature of electrochemical reaction where oxidising and reducing agents are replaced by electricity. In key studies Ania et al. studied the electro-oxidation of glucose using enzymes immobilised in carbon nanopores made by sol-gel polymerisation of resorcinol-formaldehyde mixtures and claimed promoted heterogeneous electron transfer and stable electrocatalysis of glucose oxidation [6].

* Corresponding author: email address: richard.compton@chem.ox.ac.uk

Armstrong et al. used catalytic systems where the enzymes are immobilised in nanopores formed by electrophoretic deposition of materials such as indium tin oxide (ITO) nanoparticles and reported the cycling of nicotinamide adenine dinucleotide phosphate (NADPH) and the enantioselective oxidation of alcohols [7,12,13]. They suggested that the high local concentration of NADP(H) enzymes helped increase the efficiency of cofactor recycling and realised selective oxidation of organic compounds. From a more fundamental perspective, Xia et al. insightfully studied glucose oxidation kinetics in nano-channels and asserted the possible acceleration of rate and decrease of the Michaelis-Menten constant [8,9].

A generic feature of electrochemical approaches is the necessity of modelling the electrode processes in terms of diffusion, convection, adsorption, electron transfer, chemical reaction so as to permit realistic mechanistic analysis via voltammetry and the prediction of synthetic yields in terms of kinetic, thermodynamic and transport properties. In this paper we seek to develop a theory accounting for both apparently altered (and potential dependent) Michaelis-Menten constants and for nano-confinement effects. This builds on prior models developed by Lyons [19-21] and Bartlett [22-24] but is based on bespoke, newly derived kinetic expressions which recognise the surface immobilised nature of the redox enzyme and its reaction with a solution-phase substrate, S. The full kinetic scheme addressed is shown in Figure 1. Our approach emphasises the importance of the active electrode area to the volume of the solution, especially that under nano-confinement.

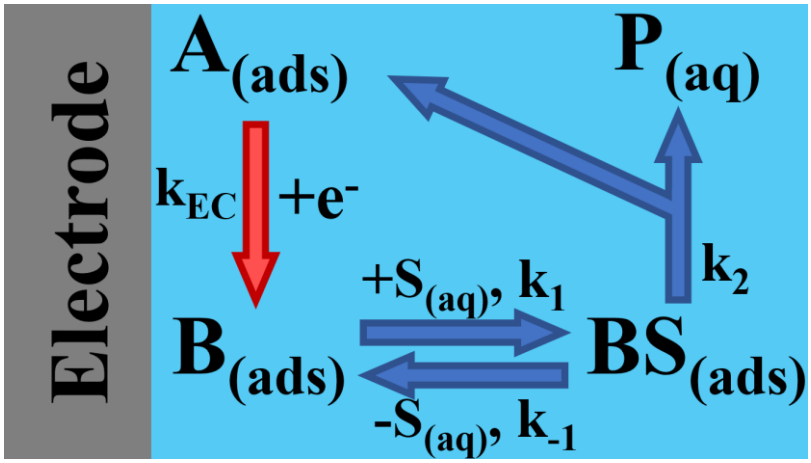

Figure 1: Illustrations of the electrode kinetics and enzyme mechanism studied in this work. The red arrow shows the electrochemical reaction for *A* to *B* on the electrode surface, while the blue arrows show the follow up chemical reactions. *A* and *B* are the oxidised and reduced forms of the enzyme, respectively, *S* is the substrate in the solution, *P* is the catalysed product, k_{EC} represents the electrochemical kinetics, k_1, k_{-1}, and k_2 are rate constants as shown in Eqn (2).

The kinetics of the enzymes in this work is described by a classical, time-invariant Michaelis-Menten-type mechanism [25,26] but adapted to recognise the biphasic nature of the reaction between an adsorbed enzyme and a solution-phase substrate. A theoretical model is presented in the next section before developing a further model of the catalytic reaction in nanopores. Unlike porous electrode model formed with parallel cylindrical pores reported by De Levie [27] or slit-like narrow cylindrical pores reported by Kornyshev *et al.* [28, 29], or rough electrode with channel-forming membranes reported by Guidelli *et al.* [30, 31], the porous electrode model in this work adopts an electrode covered with multilayers of spherical nanopores which contain solution with substrates and possess immobilised enzyme on their inner walls. Subsequently, in following sections, we

then report, interpret and discuss simulated voltammetry and its implications for practical electro-synthesis.

2 Theory

The simulation models are presented in this section with the dimensionless parameters and computational methods used. The current responses are calculated for cyclic voltammetry experiments.

2.1 The 'Non-Porous Immobilised-Enzyme' Model

The immobilised-enzyme-mediated electrochemical reaction is first modelled at a flat and non-porous planar electrode. The enzyme *A* and its reduced form *B* are assumed to be immobilised on the electrode throughout with a total enzyme coverage Γ_{max}. The bulk concentration of the substrate species *S* is set to be c_S^* and uniform before any potential is applied to the electrode. As shown in Figure 1 the reaction scheme is:

$$A_{(ads)} + e^- \rightleftharpoons B_{(ads)} \tag{1}$$

$$B_{(ads)} + S_{(aq)} \underset{k_{-1}}{\overset{k_1}{\rightleftarrows}} [BS]_{(ads)} \overset{k_2}{\rightarrow} A_{(ads)} + P_{(aq)} \tag{2}$$

where k_1, k_{-1} and k_2 are rate constants.

The electrode potential scans in the following way:

$$E(t) = \begin{cases} E(t_0) - \nu t & where \quad t < \dfrac{t_{sim}}{2} \\ E\left(\dfrac{t_{sim}}{2}\right) + \nu\left(t - \dfrac{t_{sim}}{2}\right) & where \quad t \geq \dfrac{t_{sim}}{2} \end{cases} \tag{3}$$

where $E(t)$ is the potential applied at t time point, $E(t_0)$ is the initial potential, t_{sim} is the total simulation time, and ν is the scan rate of the potential applied. The simulation time is chosen to correspond to that of a full, single cyclic voltammogram with a forward sweep and a reverse one.

The velocity of the electro-catalysis, υ_C, is:

$$\upsilon_C = D_S \frac{\partial c_S}{\partial x}\Big|_{x=0} = -D_P \frac{\partial c_P}{\partial x}\Big|_{x=0} = k_2 \Gamma_{BS} \tag{4}$$

where D_S, D_P, c_S and c_P are the diffusion coefficients and concentrations for species *S* and *P*, *x* is the coordinate normal to the electrode surface ($x = 0$), and Γ_{BS} is the surface coverage of species *BS*.

By applying the steady-state approximation to *BS*, $\frac{\partial \Gamma_{BS}}{\partial t} = 0$, we obtain:

$$k_1 \Gamma_B c_S|_{x=0} = (k_{-1} + k_2)\Gamma_{BS} \tag{5}$$

which leads to:

$$\Gamma_{BS} = \frac{k_1 c_S|_{x=0}}{k_{-1} + k_2} \Gamma_B = \frac{c_S|_{x=0}}{K_m} \Gamma_B \tag{6}$$

where K_m is the Michaelis-Menten constant for the catalytic reaction, and $K_m = \frac{k_{-1}+k_2}{k_1}$.

If reaction (1) is fully electrochemically reversible, according to the Nernst equation [32], we have:

$$\frac{\Gamma_A}{\Gamma_B} = e^{\theta} \tag{7}$$

where $\theta = \frac{F(E(t)-E_f^0)}{RT}$, and E_f^0 is the formal potential of the redox couple *A*/*B*. If we combine Eqns (6) and (7) with the conservation of surface coverage:

$$\Gamma_A + \Gamma_B + \Gamma_{BS} = \Gamma_{max} \tag{8}$$

we can obtain an expression for Γ_B:

$$\Gamma_B = \frac{\Gamma_{max}}{e^{\theta} + 1 + \frac{c_S|_{x=0}}{K_m}} \tag{9}$$

Therefore, we have:

$$D_S \frac{\partial c_S}{\partial x}\Big|_{x=0} = -D_P \frac{\partial c_P}{\partial x}\Big|_{x=0} = k_2 \Gamma_{BS} = \frac{k_2 \Gamma_B c_S|_{x=0}}{K_m} = \frac{k_2 \Gamma_{max} c_S|_{x=0}}{(e^{\theta} + 1)K_m + c_S|_{x=0}} \tag{10}$$

The diffusion equations for the species in the solution phase during the simulations are:

$$\frac{\partial c_S}{\partial t} = D_S \left(\frac{\partial^2 c_S}{\partial x^2}\right); \frac{\partial c_P}{\partial t} = D_P \left(\frac{\partial^2 c_P}{\partial x^2}\right) \tag{11}$$

Before the simulation starts ($t = 0$), Γ_A, Γ_B, Γ_{BS}, c_S and c_P are set as following:

$$\begin{aligned} &\text{At } x = 0: \Gamma_A = \Gamma_{max};\ \Gamma_B = 0;\ \Gamma_{BS} = 0 \\ &\text{For } 0 \le x \le x_m: c_S = c_S^*;\ c_P = 0 \end{aligned} \tag{12}$$

where the maximum simulation space x_m is chosen to depend on the total simulation time t_{sim}:

$$x_m = 6\sqrt{D t_{sim}} \tag{13}$$

where x_m is large enough so that the simulation is not affected by the far end boundary due to the Brownian motion of the solution phase [33, 34].

After the potential is applied ($t > 0$), at the electrode surface ($x = 0$):

$$\Gamma_A = \frac{e^{\theta}\Gamma_{max}}{e^{\theta}+1+\frac{c_S|_{x=0}}{K_m}}; \Gamma_B = \frac{\Gamma_{max}}{e^{\theta}+1+\frac{c_S|_{x=0}}{K_m}}; \Gamma_{BS} = \frac{c_S|_{x=0}}{K_M}\frac{\Gamma_{max}}{e^{\theta}+1+\frac{c_S|_{x=0}}{K_m}} \tag{14}$$

$$D_S \frac{\partial c_S}{\partial x}\Big|_{x=0} = -D_P \frac{\partial c_P}{\partial x}\Big|_{x=0} = k_2 \Gamma_{BS} = \frac{k_2 \Gamma_{max} c_S|_{x=0}}{(e^{\theta} + 1)K_m + c_S|_{x=0}} \tag{15}$$

and in the bulk of the solution phase ($x = x_m$):

$$\frac{\partial c_S}{\partial x}\Big|_{x_m} = \frac{\partial c_P}{\partial x}\Big|_{x_m} = 0 \tag{16}$$

Therefore, we can calculate the catalytic current I_C by:

$$I_C = -FA_e J_C = -FA_e D_S \frac{\partial c_S}{\partial x}\Big|_{x=0} = -\frac{FA_e k_2 \Gamma_{max} c_S|_{x=0}}{(e^{\theta} + 1)K_m + c_S|_{x=0}} \tag{17}$$

where J_C is the catalytic flux, and A_e is the electrode area. Moreover, the A/B current I_A can be calculated by:

$$I_A = FA_e J_A = FA_e \frac{\partial \Gamma_A}{\partial t} \tag{18}$$

where J_A is the flux for the *A*/*B* electrochemical reaction. Therefore, we have the total current I_T as:

$$I_T = I_C + I_A = -\frac{FA_e k_2 \Gamma_{max} c_S|_{x=0}}{(e^{\theta} + 1)K_m + c_S|_{x=0}} + FA_e \frac{\partial \Gamma_A}{\partial t} \tag{19}$$

2.1.1 Dimensionless Parameters

Dimensionless parameters are introduced to generalise the output of the simulations and to economise on simulation times [34]. In the 'immobilised-enzyme' model, the conversion from dimensional parameters to their dimensionless counterparts are shown in Table 1.

Table 1: Transformation of dimensional parameters to dimensionless parameters in the 'non-porous immobilised-enzyme' model, where ***R*** is the Universal Gas Constant, and ***T*** is the temperature.

Dimensional Parameters	Dimensionless Forms	Conversions
Concentration of species j $c_j/(mM)$	C_j	$C_j = \frac{c_j}{c_S^*}$
Surface coverage of species j $\Gamma_i/(mol\ m^{-2})$	ξ_i	$\xi_i = \frac{\Gamma_i}{\Gamma_{max}}$
Diffusion coefficient of species j $D_j/(m^2\ s^{-1})$	d_j	$d_j = \frac{D_j}{D_S}$
Distance $x/(m)$	X	$X = \frac{x}{x_m}$
Time $t/(s)$	T	$T = \frac{t}{t_{sim}}$
Scan rates $\nu/(V\ s^{-1})$	σ	$\sigma = \frac{Ft_{sim}}{\boldsymbol{RT}}\nu$
Potential $E/(V)$	θ	$\theta = \frac{F}{\boldsymbol{RT}}(E - E^0_{f,A/B})$
BS decomposition rate constant $k_2/(s^{-1})$	K_2	$K_2 = \frac{x_m\Gamma_{max}}{D_S c_S^*}k_2$
Michaelis-Menten Constant $K_m/(mM)$	K_{mm}	$K_{mm} = \frac{K_m}{c_S^*}$
A/B Flux $J_A/(mol\ s^{-1}\ m^{-2})$	j_A	$j_A = \frac{t_{sim}}{\Gamma_{max}}J_A$
Catalytic Flux $J_C/(mol\ s^{-1}\ m^{-2})$	j_C	$j_C = \frac{x_m}{D_S c_S^*}J_C$

The dimensionless diffusion equations are:

$$\frac{\partial C_S}{\partial T} = \frac{d_S}{36}\left(\frac{\partial^2 C_S}{\partial X^2}\right); \frac{\partial C_P}{\partial T} = \frac{d_P}{36}\left(\frac{\partial^2 C_P}{\partial X^2}\right) \tag{20}$$

and the dimensionless expressions for the boundary conditions before the simulation starts ($T = 0$) become:

$$\begin{aligned} &\text{At } X = 0\text{: } \xi_A = 1;\ \xi_B = 0;\ \xi_{BS} = 0 \\ &\text{For } 0 \le X \le 1\text{: } C_S = 1;\ C_P = 0 \end{aligned} \tag{21}$$

As the simulation starts ($T > 0$), at the electrode surface ($X = 0$):

$$\xi_A = \frac{e^\theta}{e^\theta + 1 + \frac{C_S|_{X=0}}{K_{mm}}};\ \xi_B = \frac{1}{e^\theta + 1 + \frac{C_S|_{X=0}}{K_{mm}}};\ \xi_{BS} = \frac{C_S|_{X=0}}{K_{mm}}\frac{1}{e^\theta + 1 + \frac{C_S|_{X=0}}{K_{mm}}} \tag{22}$$

$$d_S\left.\frac{\partial C_S}{\partial X}\right|_{X=0} = -d_P\left.\frac{\partial C_P}{\partial X}\right|_{X=0} = \frac{K_2 C_S|_{X=0}}{(e^\theta + 1)K_{mm} + C_S|_{X=0}} \tag{23}$$

and in bulk solution ($X = 1$):

$$\left.\frac{\partial C_S}{\partial X}\right|_{X=1} = \left.\frac{\partial C_P}{\partial X}\right|_{X=1} = 0 \tag{24}$$

We can relate the dimensional catalytic current I_C to the dimensionless flux j_C by:

$$I_C = -\frac{FA_e D_S c_S^*}{x_m}j_C = -\frac{FA_e D_S c_S^*}{x_m}\frac{K_2 C_S|_{X=0}}{(e^\theta + 1)K_{mm} + C_S|_{X=0}} \tag{25}$$

where $j_C = d_S\left.\frac{\partial C_S}{\partial X}\right|_{X=0}$. Similarly, we can relate the dimensional A/B current I_A to the dimensionless flux j_A by:

$$I_A = \frac{FA_e\Gamma_{max}}{t_{sim}} j_A = \frac{FA_e\Gamma_{max}}{t_{sim}} \frac{\partial \xi_A}{\partial T} \tag{26}$$

where $j_A = \frac{\partial \xi_A}{\partial T}$. The dimensional total current I_T is:

$$I_T = I_C + I_A = -\frac{FA_e D_S c_S^*}{x_m} \frac{K_2 C_S|_{X=0}}{(e^\theta + 1)K_{mm} + C_S|_{X=0}} + \frac{FA_e\Gamma_{max}}{t_{sim}} \frac{\partial \xi_A}{\partial T} \tag{27}$$

Eqn (27) is interesting. The first term corresponding to I_C indicates the role of the Michaelis constant in controlling the rate of turnover of *S* into *P*. As in conventional Michaelis-Menten kinetics, the constant K_m appears in the denominator of the expression. However, in contrast to the kinetics describing purely homogeneous enzyme kinetics, the impact of the Michaelis constant is moderated by the factor $(e^\theta + 1)$ where the exponential term describes the role of the electrode potential. For very negative potentials the factor tends to unity corresponding to the case where all the immobilised enzyme on the surface is available for binding to the substrate *S*. At less negative potentials the factor is greater than unity so that the product $(e^\theta + 1)\ K_m > K_m$ corresponding to an apparent weaker binding of *B* and *A* arising since not all the immobilised enzyme is present on the form *B*. The composite term, $(e^\theta + 1)\ K_m$, can be thought of as the *effective Michaelis constant* and explains the potential-dependent apparent K_m values observed as discussed above.

2.2 The 'Nanopore' Model

Next we consider the same enzyme-mediated process where the electrode is covered by a layer of nanopores which contain solution and where the reaction of *S* takes place on the conductive walls of the pores via the reactions Eqn (1) and Eqn (2). Again, the applied potential follows Eqn (3), and, before the reactions start, the initial surface coverages and concentrations follow Eqn (12).

Consider a single pore of volume *V* and internal surface area A_S. We assume the electrolysis within the nanopore is "thin layer" [32, 35, 36]:

$$\sqrt[3]{V} \ll \sqrt{D\frac{\boldsymbol{RT}}{F\nu}} \tag{28}$$

where ν is the scan rate (*V/s*). Then, c_S is assumed to be uniform within the cell throughout the voltammetry. Note that for a sweep rate of 0.1 *V/s* and $D = 10^{-5}$ cm^2/s, we have $\sqrt{D\frac{\boldsymbol{RT}}{F\nu}}$ at about 16 μm which is much greater than the radius of typical "nano" pores.

We therefore have:

$$\frac{\partial c_S|_{x=0}}{\partial t} = -\frac{\partial c_P|_{x=0}}{\partial t} = -k_2\Gamma_{BS} \cdot \frac{A_S}{V} = -\frac{\frac{k_2 A_S \Gamma_{max}}{V} \cdot c_S|_{x=0}}{(e^\theta + 1)K_m + c_S|_{x=0}} \tag{29}$$

Similarly, the total current in this model can be calculated by:

$$I_{PT} = I_{PC} + I_{PA} \tag{30}$$

where:

$$I_{PC} = FN_t V J_{PC} = FN_t V \frac{\partial c_S|_{x=0}}{\partial t} \tag{31}$$

$$I_{PA} = FN_t A_S J_{PA} = FN_t A_S \frac{\partial \Gamma_A}{\partial t} \tag{32}$$

where Γ_A can be calculated by Eqn (14), N_t is the total number of nanopores in the nanoporous layer, J_{PC} and J_{PA} are the catalytic flux and *A*/*B* reaction flux, respectively. Please refer to Section S2 in Supplementary Information for the calculations of N_t, A_S and *V*. Note again the appearance of the effective Michaelis constant, $(e^{\theta} + 1)\, K_m$, in Eqn (29).

2.2.1 Dimensionless Parameters

In this model, the conversion from dimensional parameters to the dimensionless ones are shown in Table 2.

Table 2: Transformation of dimensional parameters to dimensionless parameters where r_r is the radius of the nanopores. Note that the dimensionless conversions for c_j, Γ_j, D_j, x, E, and K_m are the same as those in Table 1 with x_m being replaced by r_r for conversion of x.

Dimensional Parameters	Dimensionless Forms	Conversions
Time $t/(s)$	T	$T = \frac{D_S}{r_r^2} t$
Scan rates $\nu/(V\ s^{-1})$	σ	$\sigma = \frac{r_r^2}{D_S} \frac{F}{\boldsymbol{RT}} \nu$
BS decomposition rate constant $k_2/(s^{-1})$	K_2'	$K_2' = \frac{A_S \Gamma_{max} r_r^2}{V c_s^* D_S} k_2$
A/B Flux $J_{PA}/(mol\ s^{-1}\ m^{-2})$	j_{PA}	$j_{PA} = \frac{r_r^2}{\Gamma_{max} D_S} J_{PA}$
Catalytic Flux $J_{PC}/(mol\ s^{-1}\ m^{-2})$	j_{PC}	$j_{PC} = \frac{r_r^2}{D_S c_s^*} J_{PC}$

Before the simulation starts ($T = 0$), ξ_A, ξ_B, ξ_{BS}, C_S and C_P are set as shown in Eqn (21). Note that in this model C_S and C_P are assumed to always be uniform within the nanopores. As the simulation starts ($T = 0$), at the electrode surface ($X = 0$), ξ_A, ξ_B, ξ_{BS} follow Eqn (22). C_S and C_P within the nanopores follow:

$$\frac{\partial C_S|_{x=0}}{\partial T} = -\frac{\partial C_P|_{x=0}}{\partial T} = -\frac{K_2' C_S|_{X=0}}{(e^{\theta} + 1) K_{mm} + C_S|_{X=0}} \tag{33}$$

We can relate the dimensional catalytic current I_{PC} to the dimensionless flux j_{PC} by:

$$I_{PC} = \frac{FN_t V c_S^* r_r^2}{D_S} j_{PC} = -\frac{FN_t V c_S^* r_r^2}{D_S} \frac{K_2' C_S|_{X=0}}{(e^{\theta} + 1) K_{mm} + C_S|_{X=0}} \tag{34}$$

where $j_{PC} = \frac{\partial C_S|_{X=0}}{\partial T}$. Similarly, we can relate the dimensional A/B current I_{PA} to the dimensionless flux j_{PA} by:

$$I_{PA} = \frac{FN_t A_S \Gamma_{max} r_r^2}{D_S} j_{PA} = \frac{FN_t A_S \Gamma_{max} r_r^2}{D_S} \frac{\partial \xi_A}{\partial T} \tag{35}$$

where $j_{PA} = \frac{\partial \xi_A}{\partial T}$. The dimensional total current I_{PT} is:

$$I_{PT} = I_{PC} + I_{PA} = -\frac{FN_t V c_S^* r_r^2}{D_S} \frac{K_2' C_S|_{X=0}}{(e^{\theta} + 1) K_{mm} + C_S|_{X=0}} + \frac{FN_t A_S \Gamma_{max} r_r^2}{D_S} \frac{\partial \xi_A}{\partial T} \tag{36}$$

2.3 Computational Methods

The simulation of the 'immobilised-enzyme' model was developed in *C++*, and the results were processed via *Python* using the *NumPy* and *matplotlib* libraries. The diffusion equations were solved using matrices resulting from a finite difference formulation together with the Thomas Algorithm [37–39]. Please refer to the textbook [34] for more details.

The simulation of the 'nanopore' model was developed in *Python*, and the simulation results were processed via *Python* using the *NumPy* and *matplotlib* libraries.

Testing and validation [40–42] were performed including studies of error of mass conservation and convergence, which are shown in the Supplementary Information.

3 Results and Discussion

In this section, we present and interpret the simulation results for the cyclic voltammetric response of both models and then evaluate the possible influence of nano-porosity on the electrochemistry of enzyme-mediated redox reactions and the implications for practical electrosynthesis.

In discussing the various voltammograms, references are made in the following discussions to several limits familiar from the voltammetry of flat, non-porous electrodes. First, we note that the maximum steady-state current [43] for an electrode modified with *A* arising from the reduction of *S* is:

$$I_{mss} = FA_e k_2 \Gamma_{max} \tag{37}$$

Second, the case of the *A*/*B* system immobilised on a flat electrode with no reaction with *S* leads, for the case of reversible electrode kinetics, to a symmetrical 'thin-layer' type cyclic voltammogram for which the forward peak current is [44,45]:

$$I_{tlc} = \frac{F^2 A_e \nu \Gamma_{max}}{4\boldsymbol{RT}} \tag{38}$$

Third, if the enzyme reaction is so efficient that the electrolysis of *S* is under diffusion control, the forward peak current can be calculated from the Randle-Sevcik equation for a fully reversible one-dimensional macroelectrode system [46, 47]:

$$I_{RS} = 0.446FA_e c_S^* \sqrt{\frac{FD\nu}{\boldsymbol{RT}}} \tag{39}$$

For a reductive electrochemical reaction, these three limiting cases are illustrated in Figure 2.

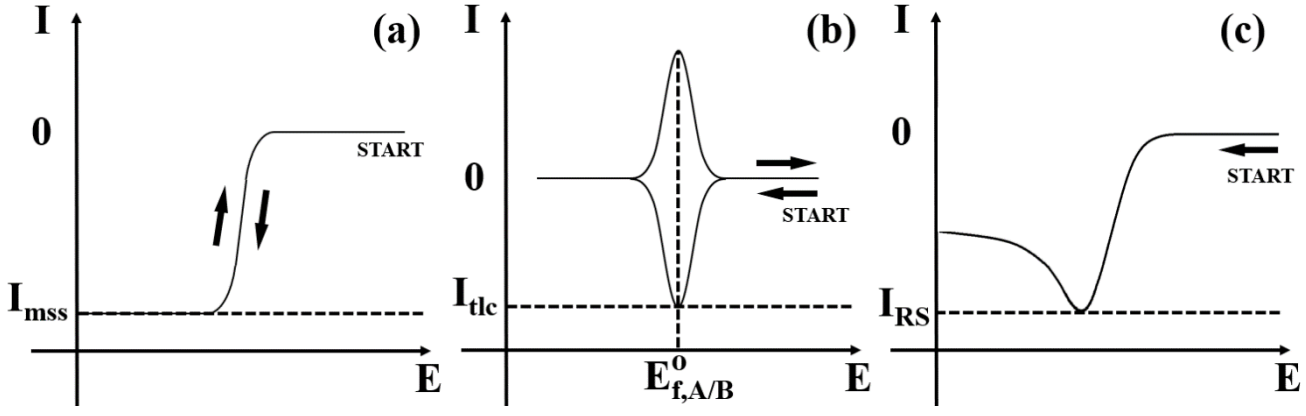

Figure 2: Illustration of the currents (a) I_{mss}, (b) I_{tlc} and (c) I_{RS} defined by Eqn (37), Eqn (38) and Eqn (39), respectively and the associated voltammetry. In this figure and figures below, the black arrows indicate the direction of scans of the cyclic voltammograms.

3.1 The 'Non-Porous Immobilised-Enzyme' Model

Simulations were carried out varying k_2, K_m, c_S* and ν to investigate the nature and trends of the voltammetry of the immobilised-enzyme-mediated electrochemical reaction at a flat and non-porous planar electrode.

Initially various simulations were computed for a series of combinations of k_2 and K_m to investigate the trends of the cyclic voltammograms based on the experimental parameters shown in Table 3, where c_S*, Γ_{max}, D_S and v were selected based on commonly used experimental conditions [48-50] from which x_m and t_{sim} were calculated. Currents are reported as current densities I_d (A/m^2) to ultimately obtain comparable results between models.

Table 3: The dimensional parameters set used in the 'non-porous immobilised-enzyme' model

Dimensional Parameter	Value
Initial Concentration of S, c_S^*	$1\ mM$
Initial Surface Coverage of A, Γ_{max}	$10^{-6}\ mol\ m^{-2}$
Diffusion Coefficient of S, D_S	$10^{-9}\ m^2\ s^{-1}$
Scan Rate, v	$2.57 \times 10^{-2}\ V\ s^{-1}$
Simulation Distance, x_m	$2.08 \times 10^{-3}\ m$
Simulation Time, t_{sim}	$120\ s$

In general, the current responses were found to approximate to one of four limiting cases, shown in Figure 3, which can be understood with reference to the catalytic mechanism, Eqn (1) and Eqn (2), as follows.

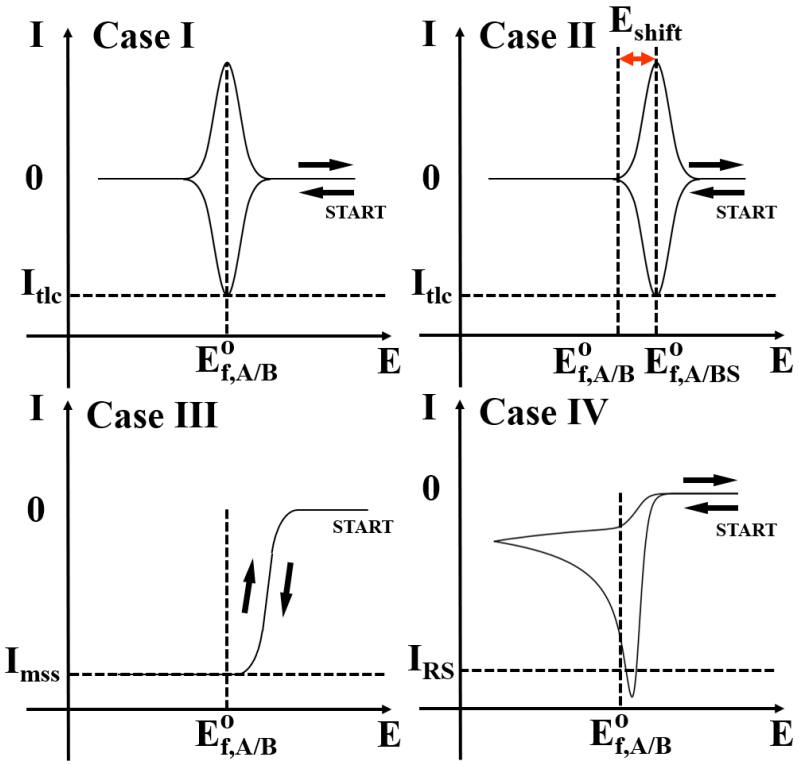

Figure 3: Illustrations of four limiting cases under extreme conditions for the cyclic voltammetry for the 'Non-Porous Immobilised-Enzyme' model.

In Case I, the binding of the substrate, S, to the active form of the enzyme B is negligible, corresponding to the limit where $K_m >> c_S$, and k_2 is so small that the voltammogram reflects the equilibrium:

$$A_{(ads)} + e^- \rightleftharpoons B_{(ads)} \tag{40}$$

The voltammetry resembles that in Figure 3, Case I where the charge passed under each of the forward and backward peaks is the same and reflects the total coverage Γ_{max}. The peak currents are close to I_{tlc} as shown in Eqn (38), and the peak potentials correspond to the formal potential of the A/B couple, $E^o_{f,A/B}$, which is set at zero in the simulations reported below.

In Case II, enzyme *B* binds the substrate *S* strongly, $K_m << c_S$, but the rate constant for decomposition of *BS*, k_2, is sufficiently tiny, $k_2 << vF/\boldsymbol{RT}$, that the voltammetry, shown in Figure 3, Case II, reflects the equilibria:

$$A_{(ads)} + e^- \rightleftharpoons B_{(ads)} \tag{41}$$

$$B_{(ads)} + S_{(aq)} \rightleftharpoons [BS]_{(ads)} \tag{42}$$

In this case, the voltammetry is similar to what is seen in Case I, with nearly symmetrical forward and reverse waves but in this limit both peaks are shifted to more positive potentials by an extent reflecting the strength of the binding given by K_m. The shift, E_{shift}, in peak potential E_{peak} which is given by:

$$E_{shift} = E_{peak} - E^o_{f,A/B} \tag{43}$$

reflects the formal potential of *A*/*BS* redox couple, $E^o_{f,A/BS}$ relative to that of $E^o_{f,A/B}$where in the case that $K_m << c_S$* corresponding to strong binding of *S* with *B*:

$$E_{peak} = E^o_{f,A/BS} + \frac{RT}{F}\ln c_S^* \tag{44}$$

where $E^o_{f,A/BS}$ relates to the half-cell reaction:

$$A_{(ads)} + S(aq) + e^- \rightleftharpoons BS_{(ads)} \tag{45}$$

so that the peak potential, E_{peak}, varies by ~59 mV (2.303$\boldsymbol{RT}/\boldsymbol{F}$) per decade of c_S* at 25 °C.

In Cases III and IV, $K_m << c_S$, and k_2 is larger than in Case II. The voltammetry resembles the full mechanism shown in Eqn (1) and Eqn (2). In Case III, as shown in Figure 3, Case III, but k_2 is not large enough to significantly deplete *S* local to the electrode so that the total mechanism is under kinetic control with the concentration of *S* remaining nearly constant; quantitatively, $k_2\Gamma_{max} << D_S^{0.5}\, c_S^*(vF/\boldsymbol{RT})^{0.5}$. Therefore, the voltammogram shows steady-state behaviour and has a limiting current as shown in Eqn (37). The half-wave potential is again shifted anodically relative to $E^o_{f,A/B}$.

In Case IV, k_2 is large enough, where $k_2\,\Gamma_{max} >> D_S^{0.5}\, c_S^*(vF/\boldsymbol{RT})^{0.5}$, so that there is significant depletion of *S* near the electrode and the voltammetry is under diffusion control and the forward voltammetric scan has a peak as shown in Figure 3, Case IV. The forward peak potential is shifted to a more positive potential relative to $E^o_{f,A/B}$ depending on the value of $E^o_{f,A/BS}$ or, equivalently, K_m. Note that there is no backward peak in this case since the formation of *P* is chemically irreversible. The following sections illustrate the transition between the different cases as various parameters are varied

3.1.1 Varying the rate constant, k_2 and the Michaelis constant, K_m

Illustrative voltammograms are presented in Figures 4 and 5 in each plot of which one of either k_2 or K_m was fixed while the other was varied. In Figure 4a, k_2 was fixed at 1 s^{-1}, and K_m was set at 10^{-2}, 10^{-1}, 10^0 and 10^1 *mM* with c_S* fixed at 1 *mM*. The currents are compared to I_{mss} and I_{tlc}. On the forward scans, all four voltammograms start from zero current corresponding to potentials which are insufficient to reduce *A* to *B*. As the potentials are swept negative, currents onset at potentials which are progressively less negative as K_m decrease corresponding to enhanced binding with *S* which is set at a concentration of 1 *mM* throughout at the beginning of simulations. Thus, for high values of K_m relative to c_S*, a simple voltammogram corresponding almost to the reversible adsorbed *A*/*B* couple is seen (red line in Figure 4a) in terms of the peak potential (corresponding to that of $E^o_{f,A/B}$

set at 0 V in the simulations). This corresponds to the Case I limit. As K_m is decreased, the backward peak is reduced in size due to the absence of enzyme in the reduced form *B* on the reverse sweep and a non-zero steady current develops at negative potentials which increases as K_m decreases ultimately maximising at a current value controlled by k_2 and given by Eqn (37) (blue line in Figure 4a). This reflects limiting Case III.

In Figure 4b, k_2 was fixed at 1000 s^{-1}, and K_m was set at 10^{-2}, 10^{-1}, 10^{0} and 10^{1} *mM* with c_S* again fixed at 1 mM. The currents were compared to I_{RS} calculated for v = 25.7 *mV/s*. On the forward scans, all four voltammograms start from zero current where the potentials are not negative enough to reduce *A*. The potentials are then swept negative where *A* starts to be reduced, and currents onset at different potentials with relatively more positive potentials observed for smaller K_m. The substrate *S* close to the electrode is depleted as potentials sweep negative for each voltammogram since the large k_2 enables rapid catalytic reaction of *S* which produces a diffusive forward peak in each plot voltammogram and corresponds to the limiting Case IV. For higher values of K_m relative to c_S*, the peak potential is observed to approach $E^o_{f,A/B}$ (red line in Figure 4b) whereas for small values of K_m the peak potential is shifted to more positive potentials due to the stronger binding of *S* (blue line in Figure 4b). The forward currents are increased for a smaller K_m and the reach a limiting value at high overpotential reflecting the value of k_2. The expected value of I_{mss} is 98.5 A/m^2. On the backward scan, there is no peak for any K_m value since conversion to *P* is irreversible.

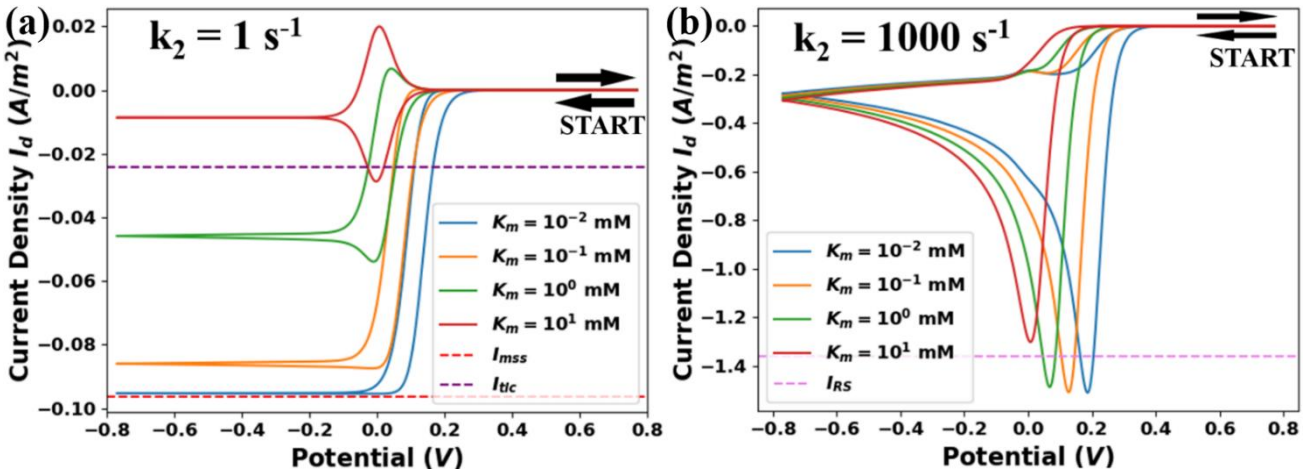

Figure 4: Voltammograms simulated varying K_m for (a) k_2 = 1 s^{-1} and (b) k_2 = 1000 s^{-1} for the 'Non-Porous Immobilised-Enzyme' model. The simulated current responses are shown in solid lines while the reference equations are shown in dashed lines. The calculated value of I_{mss} is 98.5 A/m^2 in (b).

In Figure 5a, K_m was fixed at 10^{-2} *mM*, and k_2 was set at 10^{-1} to 10^{2} s^{-1} with v and c_S* again as given in Table 3. The currents were compared to I_{RS} calculated for v = 25.7 *mV/s*, I_{tlc} from Eqn (38) and I_{mss} for the pertinent k_2 values of 0.1, 1 and 10 s^{-1}, respectively. On the forward scans, all four currents start at zero current and onset at potentials which are progressively more positive as k_2 increases corresponding to a more favourable catalytic reaction as the potential sweeps negative. For very small k_2 (k_2 << vF/RT, the blue line in Figure 5a), the voltammogram has almost symmetrical forward and reverse peaks, which are near the size of I_{tlc}, both shifted to more positive potentials than $E^o_{f,A/B}$ corresponding to limiting Case II with a limiting current close to I_{mss} at high overpotentials. As k_2 increases [but subject to $k_2\Gamma_{max}$ << $D_S^{0.5}\, c_S$*($vF/\boldsymbol{RT}$)$^{0.5}$, orange line in Figure 5a], as

discussed above, the voltammogram corresponds to the limiting Case III and a limiting current is observed at high overpotential. As k_2 increases yet further a diffusive forward peak is formed reflecting the depletion of S close to the electrode. At the same time the forward peak potential shifts to more positive potentials. Thus, the voltammogram tends to the limiting Case IV as k_2 increases, and the forward peak current eventually approaches and slightly exceeds I_{RS} limiting when $k_2\Gamma_{max} >> D_S^{0.5}\, c_S^*(vF/\boldsymbol{RT})^{0.5}$ (red line in Figure 5a). The increase of current over and above that calculated from I_{RS} is characteristic of a so-called $E_{rev}C$ process in which a reversible electrode process is followed by a chemical reaction [32, 48, 49].

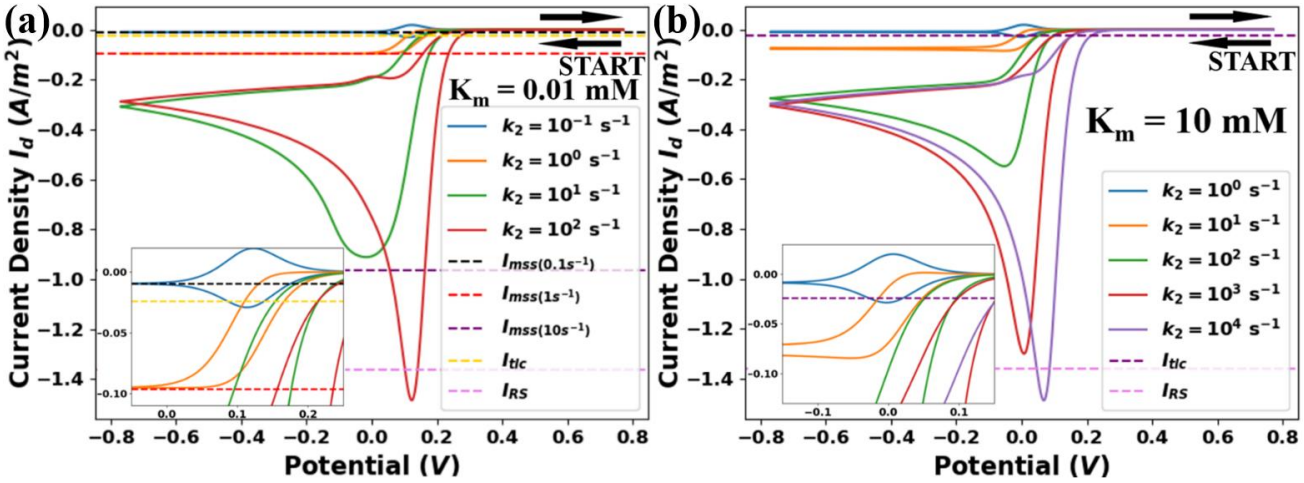

Figure 5: Voltammograms simulated varying k_2 for (a) $K_m = 10^{-2}$ *mM* and (b) $K_m = 10$ *mM*. In (a) for the 'Non-Porous Immobilised-Enzyme' model. The simulated current responses are shown in solid lines, I_{mss} is plotted for $k_2 = 0.1$ (black dashed), 1 (red dashed) and 10 (purple dashed) s^{-1}, respectively.

In Figure 5b, K_m was fixed at 10 *mM*, and k_2 was set at 10^0 to 10^4 s^{-1} with v and c_S^* as given in Table 3. The currents were compared to I_{tlc} and I_{RS} with the latter calculated for 25.7 mV/s. On the forward scans, all five currents start at zero current and catalytic currents onset at different potentials corresponding to relatively more negative potentials for smaller k_2 as the potential sweeps negative. For small k_2 ($k_2 << vF/RT$, blue line in Figure 5b), as discussed above, the voltammogram corresponds to the limiting Case I. As k_2 increases, the current on the forward scan increases but is markedly less than I_{mss}. The backward peak is reduced in size due to the absence of *B* on the reverse scan since it is in the form of *BS*. A diffusive forward peak is formed as a result of depletion of *S* close to the electrode, which again shifts the forward peak potential more positive. The voltammogram tends to resemble the limiting Case IV as k_2 increases. However, it requires a higher k_2 [$k_2\Gamma_{max} >> D_S^{0.5}\, c_S^*(vF/\boldsymbol{RT})^{0.5}$, purple line in Figure 5b], as compared to the case of the smaller K_m in Figure 5a, to exceed I_{RS} due to thermodynamically weaker binding of *S* with *B*.

3.1.2 Varying the bulk substrate concentration, c_S^*

The bulk concentration of substrate *S*, c_S^*, has a significant impact on the current responses depending on its magnitude relative to K_m. Illustrative voltammograms are presented in Figures 6 and 7 in which c_S^* was varied while k_2 and K_m were fixed. In Figure 6, c_S^* was set at 0.1, 1, 10 *mM*, K_m was fixed at 0.1 and 10 *mM* for Figures 6a and 6b, respectively, and k_2 was fixed at 1 s^{-1}. The currents are compared to I_{mss} and I_{tlc} in both plots. The plots span the full range of behaviour from negligible catalysis ($K_m = 10$ *mM*, $c_S^* = 0.1$ *mM*, blue curve in Figure

6b) corresponding to Case I through to Case III with strong catalysis under kinetic control (K_m = 0.1 *mM*, c_S* = 10*mM*, green curve in Figure 6a).

In Figure 7, c_S* was set at 0.1, 1, 10 *mM*, and K_m was fixed at 0.1 and 10 *mM* for Figures 7a and 7b, respectively, but k_2 was fixed at the higher value 1000 s^{-1} as for the Figures 6. The currents are compared to I_{RS} calculated for c_S* = 0.1, 1 and 10 *mM*. In this set of figures, the further transition into Case IV can be followed as a consequence of the increased value of k_2 in comparison with Figure 6. Thus, the development of diffusional peaks is evident in both plots in Figures 7.

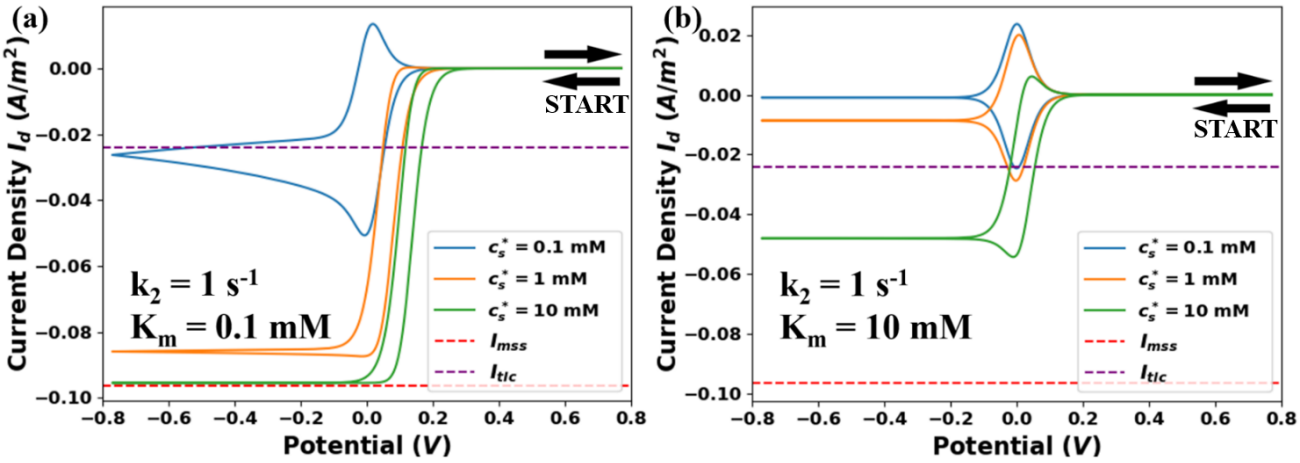

Figure 6: Voltammograms simulated at c_S* = 0.1, 1, 10 *mM* for K_m = 0.1 and 10 *mM* at k_2 = 1 s^{-1} for the 'Non-Porous Immobilised-Enzyme' model. The simulated current responses are shown in solid lines while the reference equations are shown in dashed lines.

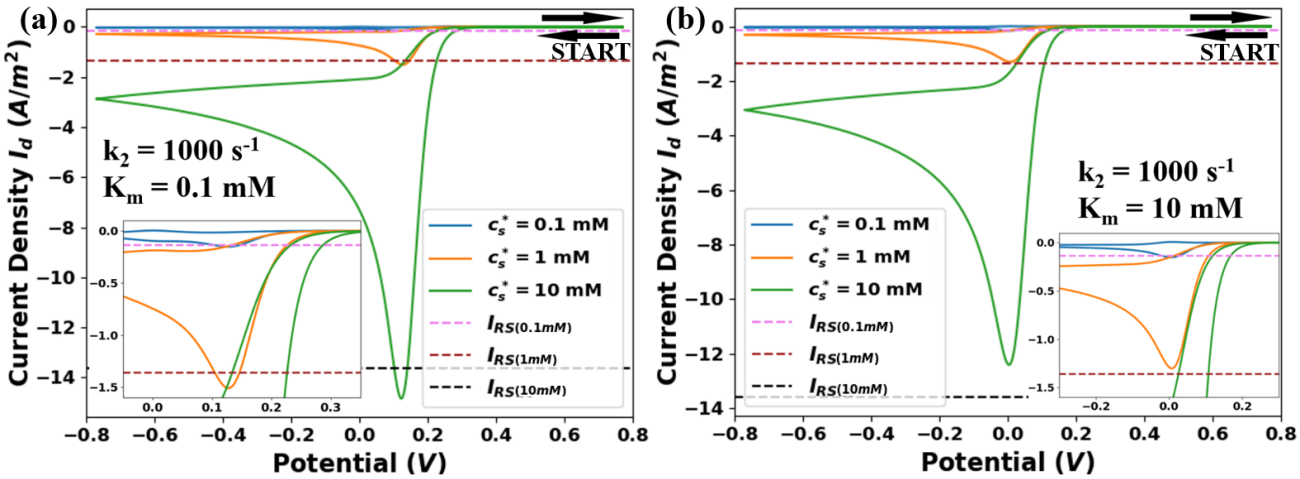

Figure 7: Voltammograms simulated at c_S* = 0.1, 1, 10 *mM* for K_m = 0.1 and 10 *mM* at k_2 = 1000 s^{-1} for the 'Non-Porous Immobilised-Enzyme' model. The simulated current responses are shown in solid lines while the reference equations are shown in dashed lines.

Further insights emerge from Table 4, which compares the values of the forward peak currents, I_p, to the corresponding I_{RS} value calculated for the pertinent concentration and gives the ratio of these two quantities as a function of different K_m and c_S* values. Note that the values of the peak currents are close to those expected for a simple diffusion-controlled process testifying to the diffusional character of the catalysed reaction. The deviation of the ratio from unity reflects two factors. First, as identified above, in the case of a reversible electron transfer process followed by irreversible chemical reaction the peak currents are expected to rise above those

predicted by the Randles-Sevcik equation for a simple one electron transfer. Second, the most effective catalysis in terms of a comparison with what is expected for a simple diffusion-controlled electrolysis, is seen for small values of K_m and low values of c_S*, even though the absolute values of the current are higher in the latter case. These factors are best seen in the data for K_m = 10 *mM* where the first factor is evident for c_S* = 0.1 *mM* whilst for c_S* = 10 *mM* the substrate concentration is comparable to the K_m value so that the catalysis is less effective and the ratio of currents drops below unity.

Table 4: Values of I_p, I_{RS} and their ratios at c_S* = 0.1, 1, 10 *mM* for K_m = 0.1 and 10 *mM* at k_2 = 1000 s^{-1}. The corresponding voltammograms are shown in Figure 7.

c_S* / *mM*	I_{RS} / (A/m^2)	K_m = 0.1 *mM*		K_m = 10 *mM*	
		I_p / (A/m^2)	I_p / I_{RS}	I_p / (A/m^2)	I_p / I_{RS}
0.1	-0.136	-0.152	1.114	-0.152	1.115
1	-1.361	-1.508	1.108	-1.301	0.956
10	-13.613	-14.841	1.090	-12.415	0.912

3.1.3 Varying the scan rate, *v*

The scan rate of the applied potential in the electrochemical processes also influences the current responses significantly. Illustrative voltammograms are presented in Figures 8 and 9 in which the scan rate, *v*, was varied while k_2 and K_m were fixed. In Figure 8, *v* was set at 2.57, 25.7, 257 *mV/s*, K_m was fixed at 0.01 and 10 *mM* for Figures 8a and 8b, respectively, and k_2 was fixed at 1 s^{-1}. The currents are compared to I_{mss} and I_{tlc} calculated at corresponding scan rates in both plots. Similar to Figure 6, the plots span the full range of behaviour from negligible catalysis to Case III with strong catalysis under kinetic control (K_m = 0.01 *mM*, *v* = 2.57 *mV/s*, blue curve in Figure 8a). However note that in Figure 8a the negligible catalysis limit (K_m = 0.01 *mM*, *v* = 257 *mV/s*, green curve in Figure 8a) corresponds to Case II with shifted peak potentials, but in Figure 8b the negligible catalysis limit (K_m = 10 *mM*, *v* = 257 *mV/s*, green curve in Figure 8b) corresponds to Case I.

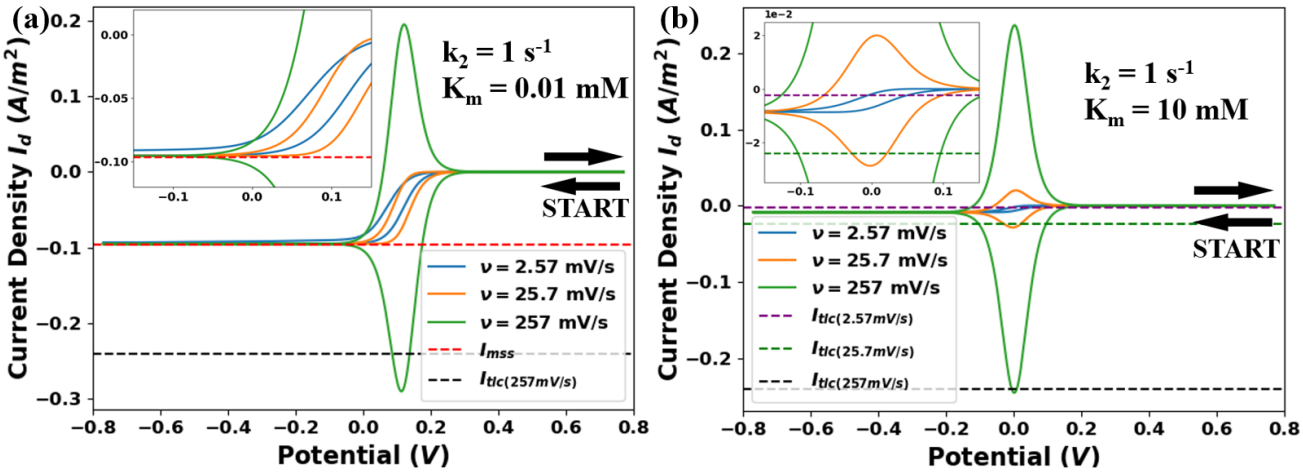

Figure 8: Voltammograms simulated at *v* = 2.57, 25.7, 257 *mV/s* for K_m = 0.01 and 10 *mM* at k_2 = 1 s^{-1} for the 'Non-Porous Immobilised-Enzyme' model. The simulated current responses are shown in solid lines while the reference equations are shown in dashed lines.

In Figure 9, *v* was set at 2.57, 25.7, 257 *mV/s*, and K_m was fixed at 0.1 and 10 *mM* for Figures 9a and 9b, respectively, but k_2 was fixed at the higher value 1000 s^{-1} as for the Figures 8. The currents are compared to I_{RS}

calculated for v = 2.57, 25.7, and 257 *mV/s*. In this set of figures the further transition to Case IV is observed due to an increased value of k_2 in comparison with Figure 8. Therefore, diffusional peaks are well developed in both Figures 9, especially at higher scan rates.

Table 5 compares the values of I_p to the corresponding I_{RS} value calculated for the pertinent scan rate and presents the ratio of these two values. Both values increase with scan rate, but the I_{RS} values increases more strongly explaining the decrease in the ratio with scan rate. Further, as discussed above, Case IV mechanism can lead to a forward peak current exceeding the peak current predicted by the Randles-Sevcik equation for a small K_m relative to c_S* whereas, for a large K_m, I_{RS} is lower than I_{RS}. The strongest relative catalysis is seen for the lowest scan rates tabulated although of course these correspond to lower absolute currents.

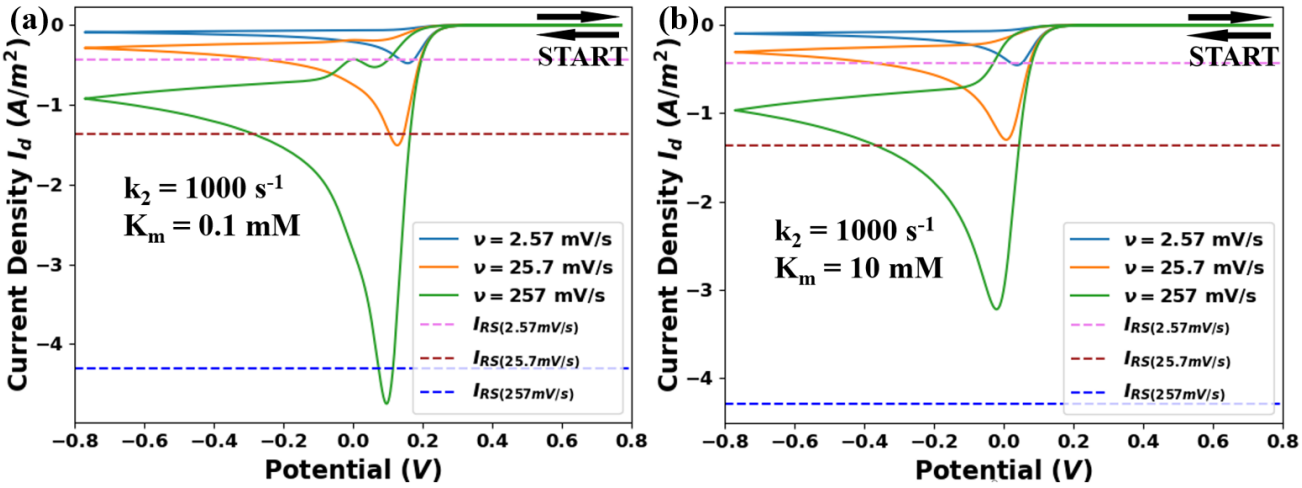

Figure 9: Voltammograms simulated at v = 2.57, 25.7, 257 *mV/s* for K_m = 0.1 and 10 *mM* at k_2 = 1000 s^{-1} for the 'Non-Porous Immobilised-Enzyme' model. The simulated current responses are shown in solid lines while the reference equations are shown in dashed lines.

Table 5: Values of I_p, I_{RS} and their ratios at v = 2.57, 25.7, 257 *mV/s* for K_m = 0.1 and 10 *mM* at k_2 = 1000 s^{-1} as shown in Figure 9.

v / (mV/s)	I_{RS} / (A/m^2)	K_m = 0.1 *mM*		K_m = 10 *mM*	
		I_p / (A/m^2)	I_p / I_{RS}	I_p / (A/m^2)	I_p / I_{RS}
2.57	-0.430	-0.478	1.110	-0.453	1.053
25.7	-1.361	-1.508	1.108	-1.301	0.956
257	-4.305	-4.751	1.104	-3.227	0.750

3.2 The 'Nanopore' Model

Calculations were carried out varying k_2, K_m, c_S* and v to investigate the features of the voltammetry for the electrochemical reaction mediated by an enzyme immobilised in a porous layer on the electrode surface using the experimental parameters shown in Table 6, where c_S*, Γ_{max}, D_S and v were, unless themselves varied, based on the values in Table 3. r_r, N_t, A_S and V were selected and calculated based on literature [7,12,13] as shown in the SI. Note that the current densities I_d (A/m^2) presented in the figures reported for this model refer to current per square meter of electrode area, ***not*** per square meter of internal area of pores.

Table 6: The dimensional parameters set used in the 'nanopore' model based in part in data reported in reference [7,12,13].

Dimensional Parameter	Value
Pore Radius, r_r	$25 \times 10^{-9}\ m$

Total Number of Nanopores per Square Meter of Electrode, N_t	$1.85 \times 10^{16}\ m^{-2}$
Internal Area of a Single Pore, A_S	$7.85 \times 10^{-15}\ m^2$
Volume of a Single Pore, V	$6.54 \times 10^{-23}\ m^3$

3.2.1 Varying the rate constant, k_2 and the Michaelis constant, K_m

In this section, k_2 and K_m are varied to investigate the shapes and trends of cyclic voltammetry for the 'nanopore' model. We first investigated the voltammograms where the catalytic effect is tiny. Illustrative voltammograms are presented in Figures 10a where k_2 was fixed at $10^{-9}\ s^{-1}$ while K_m was varied for $c_S^* = 1\ mM$.

Figure 10a shows voltammograms simulated for $K_m = 10^{-3}$ to $10^{1}\ mM$ at $k_2 = 10^{-9}\ s^{-1}$ and $c_S^* = 1\ mM$ and with the standard potential for the *A*/*B* couple fixed at 0 *V*. Note the infinitesimally slow rate constant. We observe a clear transition from Case I (purple line in Figure 10a) to Case II (blue line in Figure 10a) in the voltammograms as K_m decreases. Figure 10b, shows that as K_m decreases the peak shifts to progressively more positive values consistent with the stronger binding of *S* to *B*. Furthermore, for sufficiently small K_m, E_{peak} decreases by an amount ~59 *mV* (2.303***RT***/***F***) per decade of K_m. Conversely, as K_m increases E_{peak} approaches the standard formal potential for the *A*/*B* redox couple.

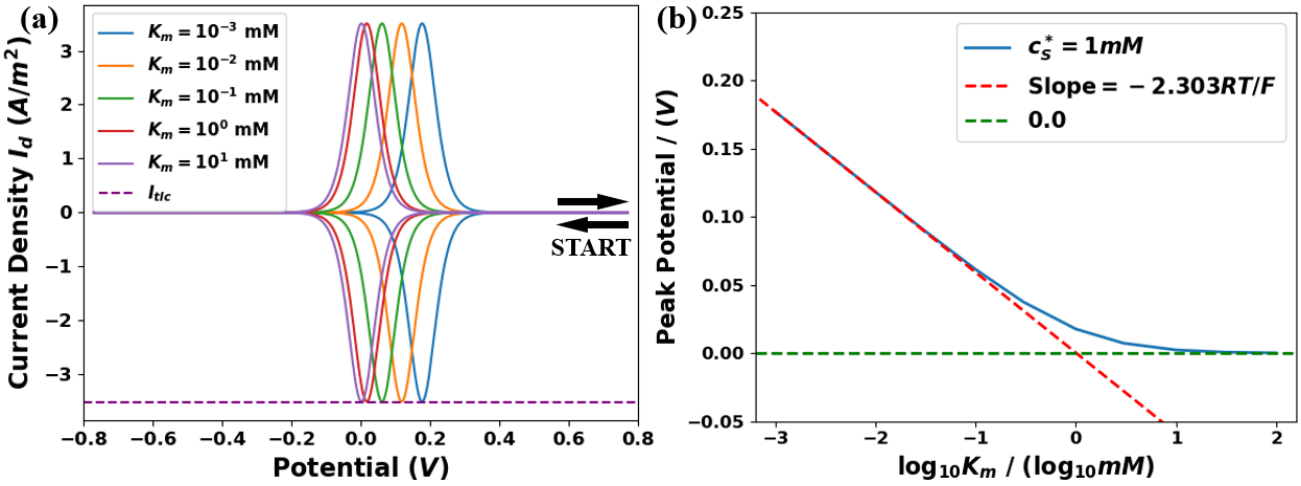

Figure 10: Voltammograms (a) and peak potentials (b) simulated for $K_m = 10^{-3}$ to $10^{1}\ mM$ at $k_2 = 10^{-9}\ s^{-1}$ and $c_S^* = 1\ mM$ for the 'Nanopore' model. Simulated current responses are shown in solid lines while the reference equations are shown in dashed lines.

Similarly, voltammograms were simulated, as shown in Figures S7-S9 in SI, varying K_m for 10^{-3} to $10^{2}\ mM$ at $k_2 = 1$, 10^3 and $10^5\ s^{-1}$ with $c_S^* = 1\ mM$. For larger k_2, introducing a stronger catalytic effect, a pre-peak will form in voltammograms before *A*/*B* redox peak at 0 *V*. The pre-peak is formed since the substrate *S* inside the nanopores is rapidly depleted as *B* forms in the electrochemical process. The peak potentials E_{peak} for the pre-peak in the forward scans were extracted and are shown in Figure 11. These can be compared with pre-peak potentials for a negligible $k_2 = 10^{-9}\ s^{-1}$ (Figure 10b). Note that for $k_2 = 1\ s^{-1}$ shown as the orange line in Figure 11, fewer points can be plotted as the pre-peak is merged with the *A*/*B* peak. As shown in Figure 11, the pre-peaks shift to more positive potentials due to increased catalytic effects for larger k_2. For $k_2 = 1$, 10^3 and $10^5\ s^{-1}$, the variations of the peak potentials for the pre-peaks follows the expected slope of ~ -59 *mV* (-2.303***RT***/***F***) per decade of K_m over the range of K_m values studied. Note that for $k_2 = 1$ and $10^3\ s^{-1}$, for sufficiently large K_m, pre-peak potentials tend to the value expected for a simple *A*/*B* peak as the binding becomes increasingly negligible.

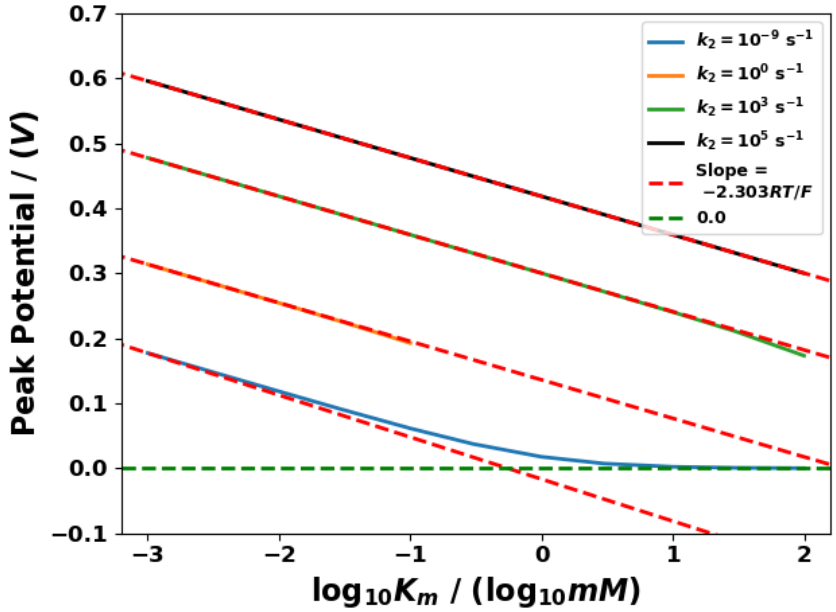

Figure 11: Peak potentials for the simulated voltammograms varying K_m at k_2 = 10^{-9}, 1, 10^3 and 10^5 s^{-1} at c_S* = 1 *mM* for the 'Nanopore' model. Simulated current responses are shown in solid lines while the reference equations are shown in dashed lines.

3.2.2 Varying the bulk substrate concentration, c_S*

Next, we varied the bulk concentration of substrate *S*, c_S*, at fixed k_2 and K_m to show its impact on the current responses. Figures 12a and 12b show the voltammetry and the variation of the peak potential for the case where the value of K_m is fixed but the substrate concentration is varied, again in the limit of infinitesimal k_2. The value of $E^o_{f,A/BS}$ is again fixed at 0 *V*. It can be seen that the simulated peak potential E_{peak} shifts to more positive potentials as c_S* increases whereas for smaller c_S*, E_{peak} tends to 0 *V*. In the limit of high c_S*, E_{peak} increases ~59 *mV* (2.303***RT***/***F***) per decade of c_S*.

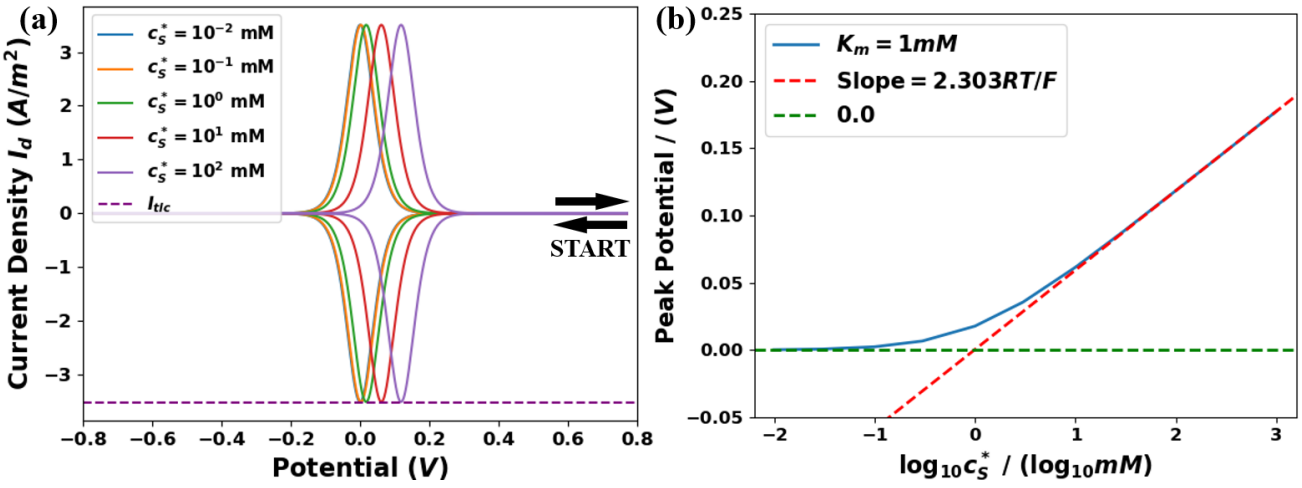

Figure 12: Voltammograms (a) and peak potentials (b) simulated for c_S* = 10^{-2} to 10^2 *mM* at k_2 = 10^{-9} s^{-1} and K_m = 1 *mM* for the 'Nanopore' model. Simulated current responses are shown in solid lines while the reference equations are shown in dashed lines.

Particularly interesting voltammetry is observed as k_2 is increased to progressively enhance the catalytic effect, so starting the transition to Case III. Figures 13a and 13b show the voltammograms simulated varying c_S* for 10^{-2} to 10^2 *mM* at k_2 = 1 and 1000 s^{-1}, respectively, with K_m = 1 *mM*. We see that, compared to Figure 12a, a

pre-peak to the main *A*/*B* peak is formed as a consequence of the catalytic reaction. For voltammograms in both Figure 13a and 13b, as c_S* increases, the size of the pre-peak current increases whilst the peak potential E_{peak} for the pre-peak in the forward scans stays near a fixed potential. For Figure 13a, the peak potentials are shifted less positively due to the relatively smaller k_2. Therefore, the pre-peak is partially merged with the *A*/*B* peak, especially for a smaller c_S* (blue line in Figure 13a) where the peak current for the pre-peak is tiny compared to the *A*/*B* peak. Furthermore, as discussed in the previous section, a peak showing oxidative currents is formed after the pre-peak for a large c_S* (purple line in Figure 13a) due to formation of *BS* in the process as shown in Figure S10 in SI. The *BS* which survives the voltammetric scan through the pre-peak is re-oxidised to *A* at potentials anodic of the formal potential of the *A*/*B* couple. For Figure 13b, for a large k_2, the pre-peaks are shifted to more positive potentials due to the stronger catalytic effect. Such observations hint at the possibility of studying the enzyme complexes *BS* voltammetrically.

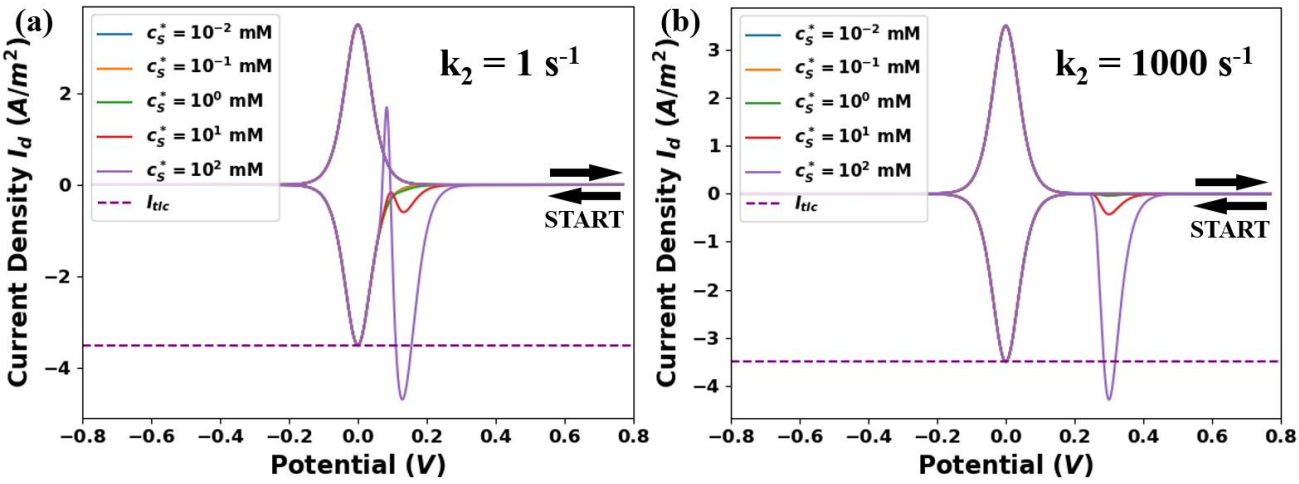

Figure 13: Voltammograms simulated for c_S* = 10^{-2} to 10^2 *mM* at k_2 = 1 and 1000 s^{-1} and K_m = 1 *mM* for the 'Nanopore' model. Simulated current responses are shown in solid lines while the reference equations are shown in dashed lines.

3.2.3 Varying scan rate *v*

Voltammograms were simulated, as shown in Figure S11-S13 in SI, varying *v* for 0.257 *mV/s* to 2.57 *V/s* at k_2 = 1, 10^3 and 10^5 s^{-1} with c_S* = 1 *mM* and K_m = 1 *mM*, and the peak potentials for the pre-peaks were extracted and plotted in Figure 14 comparing to the peak potentials for k_2 = 10^{-9} s^{-1} which is at the standard formal potential of *A*/*B* redox couple (0 *V*). For k_2 = 1 s^{-1} shown as the orange line in Figure 14, fewer points can be plotted as the pre-peak is merged with the *A*/*B* peak. Similar to Figure 11, the peak potentials of the pre-peaks shift to more positive potentials for increased k_2. For k_2 = 1, 10^3 and 10^5 s^{-1}, the varying rates of the peak potentials for the pre-peaks correspond to the expected slope of ~ -59 *mV* (-2.303***RT***/***F***) per decade of *v* over the range of *v* values studied.

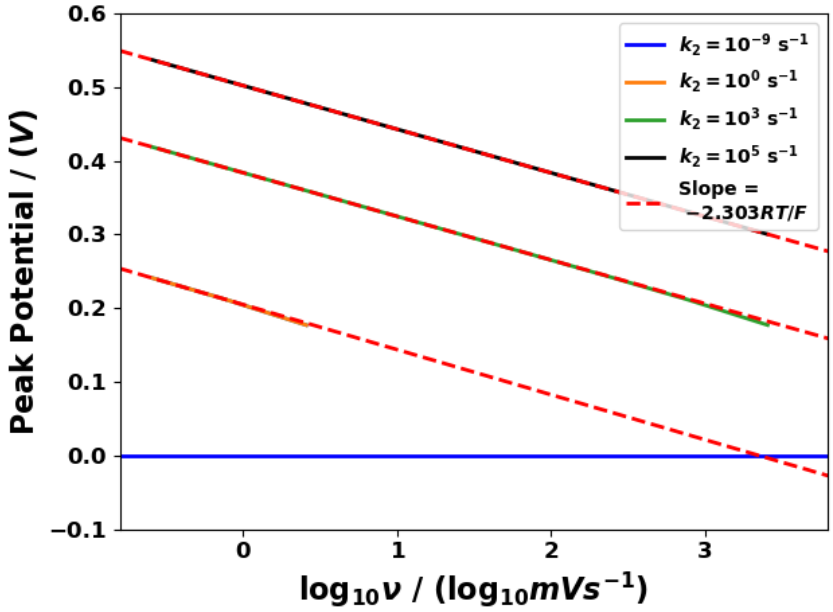

Figure 14: Peak potentials for the simulated voltammograms varying ν at k_2 = 10^{-9}, 1, 10^3 and 10^5 s^{-1} at c_S* = 1 *mM* and K_m = 1 *mM* for the 'Nanopore' model. Simulated current responses are shown in solid lines while the reference equations are shown in dashed lines.

3.3 A Comparison of Flat and Nano-Porous Electrodes: Appreciating the Role of Nanoporosity and Optimising Substrate Conversion to Product

In this section we compare the responses of the flat, non-porous electrode and a nano-porous electrode. In the first case we examine a typical macroelectrode whereas in the latter case we assume, based on the seminal work of Armstrong et al [7,12,13], that the porous layer comprises a dense network of pores of radius 25 nm within a 2-micron-thick layer on the electrode surface. We estimate (again see Section S2 in SI) that the layer comprises ca 1.85×10^{16} such pores per square metre. Note that in the model developed above the pores are considered isolated and not in diffusional communication with either each other or with the bulk solution. Nevertheless, the pore content is assumed to be solution of the same composition (concentration of *S*) as pertains in the bulk solution considered for the flat electrode. We return to these assumptions below.

In the first instance we compare these responses of the electrodes under conditions in which the enzyme is adsorbed at the same coverage on the surface of the flat macro-electrode and on the surface of each of the 1.85×10^{16} pores per square metre. We then compare the currents flowing through the same geometric area of the electrode surface. Thus, each of the pores contributes its own flux to the current density (A/m^2) of the porous electrode as a whole which is calculated by $I_{PT} = N_t A_s I_P$ (see Eqn 36). where N_t is the total number of pores per square metre, A_s is the internal area of a single pore, and I_P is the current response for a single pore. Note that the coverage chosen for these simulations approximately corresponds to ca monolayer coverage of a surface corresponding to 6.02×10^{13} molecules per square centimetre.

In Figure 15 we compare the responses for the values of K_m of either 0.1 *mM* or 10 *mM* and k_2 of either 1 s^{-1} or 1000 s^{-1} leading to the four possible cases of (Figure 15a), K_M = 10 *mM* and k_2 = 1 s^{-1} (weak catalysis) through K_m = 10 *mM* and k_2 = 1000 s^{-1} (Figure 15b), K_m = 0.1 *mM* and k_2 = 1 s^{-1} (Figure 15c) and K_m = 0.1 *mM* and k_2 =

1000 s^{-1} (Figure 15d) corresponding to increasing catalytic activity. Note that pre-peaks which are tiny on the scale of the main voltammograms in each figure are shown as amplified on the insets where the scale difference of a factor of 100 should be noted in Figures 15a, 15b and 15d.

In the four figures the transition from Case I to Case IV can be easily discerned for the planar electrode. A similar behaviour is seen for the pre-peak of the porous electrode. However, the dominant feature of the latter is that the size of the peak associated with the *A*/*B* reduction is much greater in size than the pre-peak which involves the consumption of *S*. This in turn arises because for a typical single pore the number of moles on the surface is 7.85×10^{-21} moles of *A* whereas in the volume of the pore there are 6.54×10^{-23} moles of S. Thus, the size of the immobilised feature is much greater.

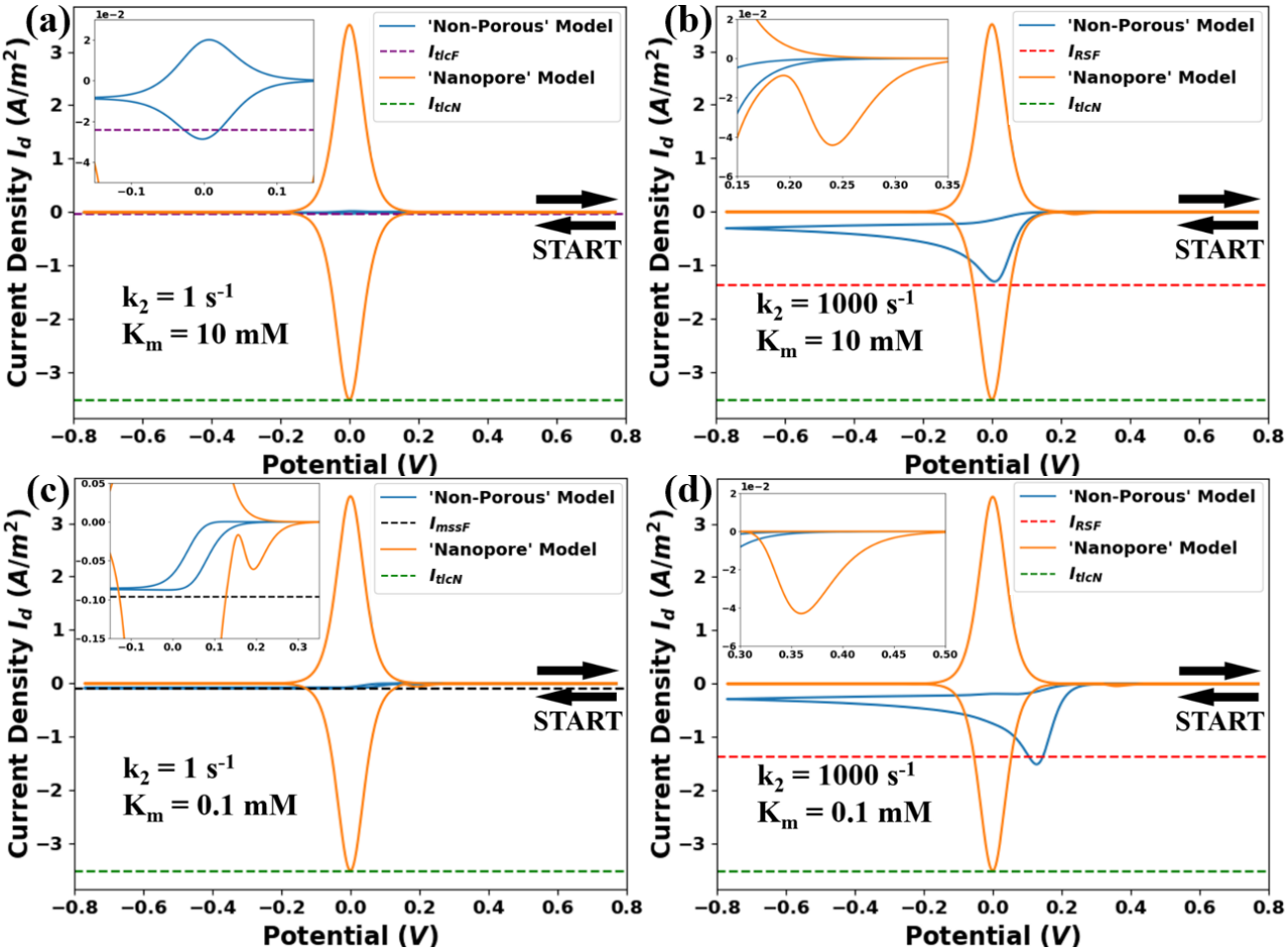

Figure 15: Voltammograms simulated for two models of K_m of either 0.1 *mM* or 10 *mM* and k_2 of either 1 s^{-1} or 1000 s^{-1} at c_S* = 1 *mM*, and v = 25.7 *mV*/*s*. Note that 'Non-Porous' Model is short for the 'Non-Porous Immobilised-Enzyme' model. I_{tlcF} and I_{tlcN} are I_{tlc} calculated for the 'Non-Porous Immobilised-Enzyme' model and the 'Nanopore' Model, respectively. I_{RSF} and I_{mssF} are the Randle-Sevcik Equation and I_{mss} calculated for the 'Non-Porous Immobilised-Enzyme' model. Initial surface coverages for enzyme *A* for both models are set to 10^{-6} mol/m^2.

In the second instance we compare the responses of flat electrodes either modified as for Figure 15 or else with a coverage corresponding to the total enzymes per geometric square metre of a porous electrode. Thus, we consider the case of an electrode with an effective loading of $N_t A_s \Gamma_A$ where Γ_A is the loading as used above. Note that this is a hypothetical case since the resulting enzyme loading is then multilayer and much greater than

monolayer. However we argue that an optimal form of porous electrode will be one in which the pores are in full or at least substantial diffusional communication with the bulk solution and hence the amount of substrate that can be converted to product is that within the diffusion layer of the electrode and not limited to the content of the pores. This offers a substantial enhancement because of the greater extent of the diffusion layer of the accessible surface in comparison with the 2-micron thickness of the porous layer. A flat electrode under conditions of semi-infinite diffusion has a diffusion layer of the size of tens or hundreds of microns depending on scan rate allowing a significant fraction of the substrate *S* within the layer to be converted into *P*.

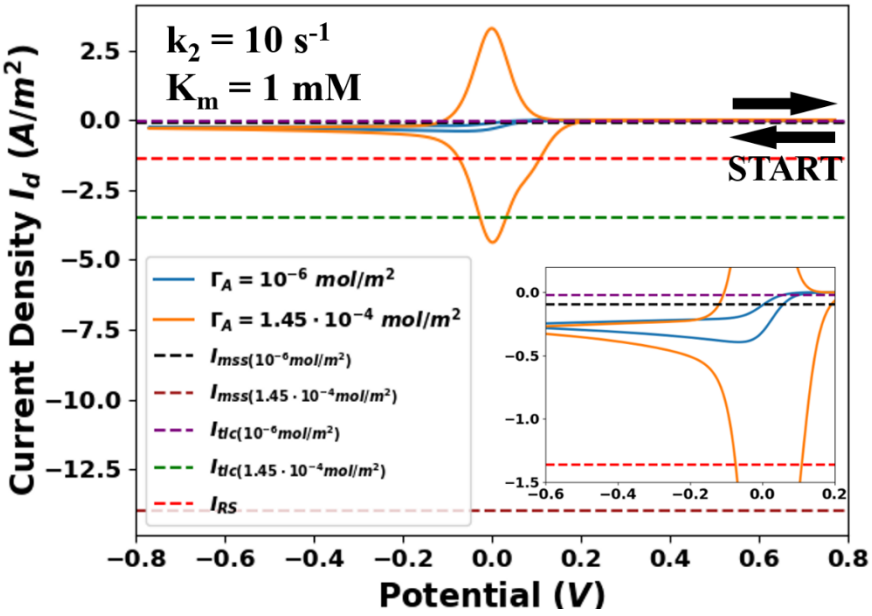

Figure 16: Voltammograms simulated for the 'Non-Porous Immobilised-Enzyme' model for $\Gamma_A = 10^{-6}$ and 1.45×10^{-4} mol/m^2 at $k_2 = 10\ s^{-1}$, $K_m = 1\ mM$, $c_S^* = 1\ mM$, and $v = 25.7\ mV/s$. The simulated current responses are shown in solid lines while the reference equations are shown in dashed lines.

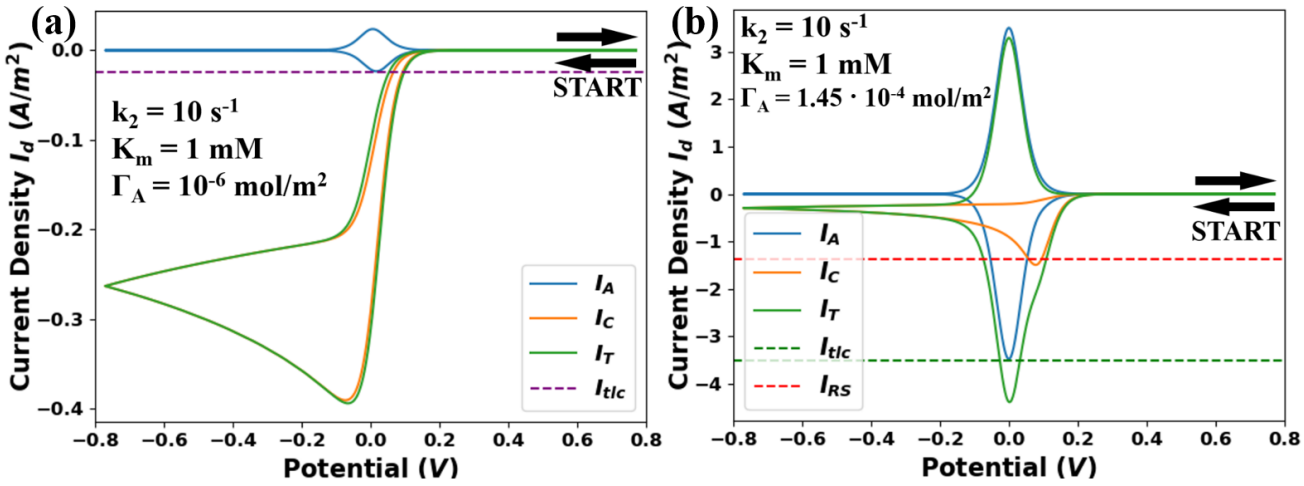

Figure 17: Voltammograms simulated including I_C, I_A and I_T from Eqns (25) – (27) for the 'Non-Porous Immobilised-Enzyme' model for (a) $\Gamma_A = 10^{-6}$ mol/m^2 and (b) $\Gamma_A = 1.45 \times 10^{-4}$ mol/m^2 at $k_2 = 10\ s^{-1}$, $K_m = 1\ mM$, $c_S^* = 1\ mM$, and $v = 25.7\ mV/s$. Simulated current responses are shown in solid lines while the reference equations are shown in dashed lines. In (b), I_{RS} is calculated to be 1.36 A/m^2.

From a diffusional perspective a fully accessible thin layer of pores can be realistically modelled as a flat electrode with an increased coverage overall average coverage to reflect the total amount of enzyme

immobilised over the *geometric* area of the electrode. With this is mind we consider the equations developed above for voltammetric response to identify those conditions under which the use of porosity to create an effective high surface coverage might be useful. Eqn (27) in particular shows first that for effective conversion of *S* to *P* (current I_C) it is essential that, in dimensional terms, K_m << [S] corresponding to the effective binding of *S* with *B* to create *BS*. In the event that the enzyme used has a relatively large K_m value then the deployment of an increased coverage Γ_A can compensate. This is illustrated by Figure 16 in which K_m = 1 mM and c_S* = 1 mM. and the voltammetric response for the two coverages 10^{-6} and 1.45×10^{-4} mol/m^2 are compared. Figures 17a and 17b show the two responses dissected into the contributions I_C and I_A. This is important since the signal from the immobilised enzyme electrochemistry (I_A) obscures the response from the substrate conversion (I_C). Importantly for the low coverage the substrate conversion is much below that expected for the diffusional discharge of *S* as estimated by the Randles-Sevcik equation for the (electrochemically reversible) discharge of *S* at a flat electrode. In contrast I_C in Figure 17b calculated for the porous electrode mimic (that is the flat electrode with a higher coverage), a near diffusional response is seen. This is because although not all the reduced enzyme, *B*, is in the form *BS* because of the high value of K_m, increasing the coverage increased the amount of *BS* present and hence the overall turnover of *S* to *P*.

Second, returning to Eqn (23), and assuming the K_m << c_S*, it is evident that if k_2, the rate constant for the decomposition of *BS*, is sluggish then again improved catalysis can be realised via the porous electrode strategy and the creation of an effective very high coverage. This is illustrated in Figure 18 where K_m = 0.1 mM and c_S* = 1 mM meeting the first criterion, but it is assumed that k_2 = 0.3 s^{-1}. Again, the responses for the high and low coverages of 10^{-6} and 1.45×10^{-4} mol/m^2 are plotted and decomposed in Figures 19a and 19b into the components I_A and I_C. It is apparent that I_C reaches the diffusional limit for the discharge of *S* with the high coverage but is substantially less for the lower coverage.

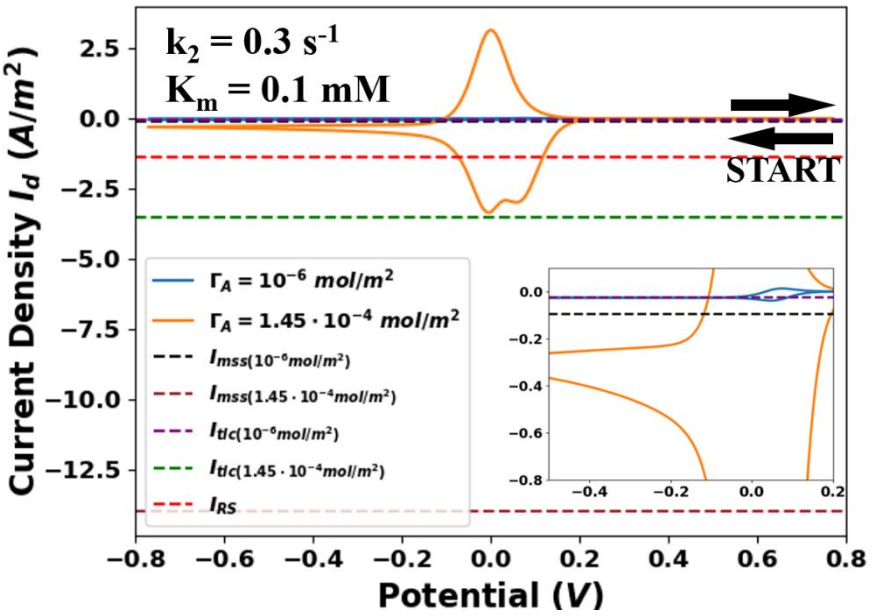

Figure 18: Voltammograms simulated for the 'Non-Porous Immobilised-Enzyme' model for Γ_A = 10^{-6} and 1.45×10^{-4} mol/m^2 at k_2 = 0.3 *s*$^{-1}$, K_m = 0.1 *mM*, c_S* = 1 *mM*, and *v* = 25.7 *mV/s*. The simulated current responses are shown in solid lines while the reference equations are shown in dashed lines.

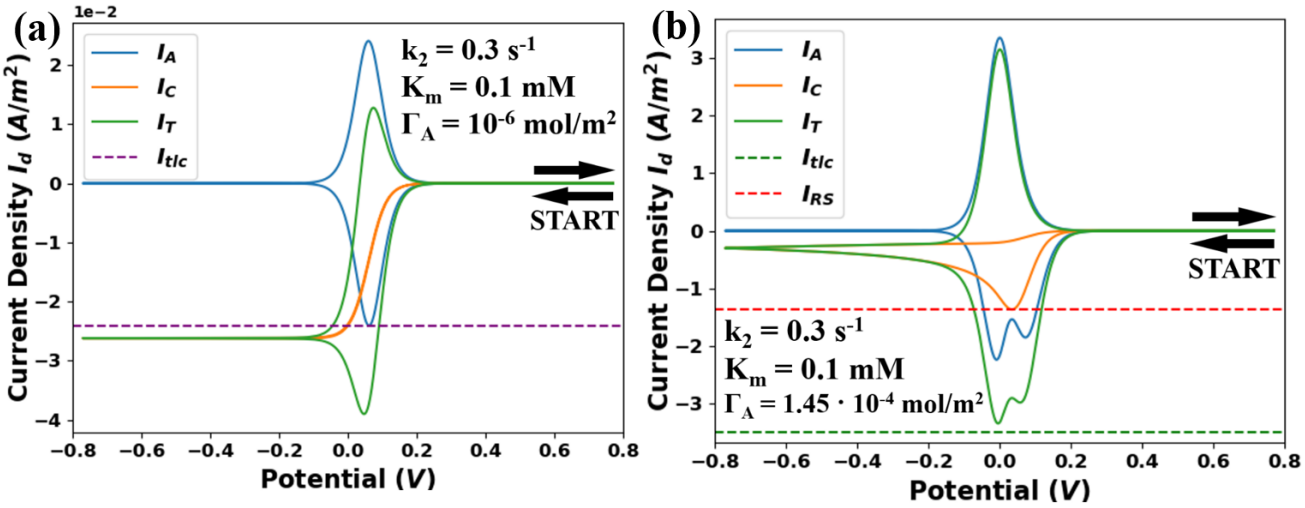

Figure 19: Voltammograms simulated including I_C, I_A and I_T from Eqns (25) – (27) for the 'Non-Porous Immobilised-Enzyme' model for (a) $\Gamma_A = 10^{-6}$ mol/m^2 and (b) $\Gamma_A = 1.45 \times 10^{-4}$ mol/m^2 at $k_2 = 0.3\ s^{-1}$, $K_m = 0.1\ mM$, $c_S^* = 1\ mM$, and $\nu = 25.7\ mV/s$. Simulated currents are shown in solid lines while the reference equations are shown in dashed lines. In (b), I_{RS} is calculated to be 1.36 A/m^2.

The above comparisons confirm the enormous potential for the use of surface porosity in creating an effective ultrahigh surface loading of enzyme which can offset limitations arising from both the thermodynamic parameters K_m and the kinetic constant k_2. However, in order for the porous layer to be effective we stress the essential need for the porous layer to have diffusional communication with the bulk solution so as to turn usefully large amount of *S* into *P*. Thus, for effective catalysis the nano-porosity needs to create surface roughness as opposed to 'nano-confinement' at least in the diffusional sense. That said, roughness at the *nano*scale is especially effective in creating the increased area need for enhanced enzyme adsorption. It is worth noting that besides the enhanced enzyme surface coverage and the different diffusion pattern in nanopores comparing to the bulk solution, the advantages of nano-confinement might originated from other effects, which could be further investigated via theoretical and experimental studies.

4. Conclusions

This work has utilised modelling and simulation tools to predict the cyclic voltammetry with immobilised-enzyme-mediated electrochemical processes on a flat electrode and on a porous electrode. The simulations were based on Fickian diffusion and Michaelis-Menten enzyme kinetics. For the model with flat electrodes, four limiting cases were identified and reflected first feeble binding between the enzyme and the substrate and negligible catalysis (Case I), second strong binding and tiny catalysis (Case II), third strong binding and significant but slow turnover (Case III), and fourth, in Case IV, strong binding and fast formation of the products. The latter case, corresponding to efficient electrochemical enzyme catalysis and leads to marked depletion of the substrate local to the electrode and hence voltammetric signals of a diffusional character which fingerprints the sought high turnover of *S*. The kinetic equations developed explain reported *apparent* potential dependence of the Michaelis constant in controlling the catalytic currents

Comparison of the flat and porous electrodes suggests that the latter best operate when in diffusional communication with the bulk solution and serve to create an effective high surface coverage of enzyme on the

electrode surface. The conditions under which this is beneficial shown to be either where the Michaelis constant shows less than strong binding to the substrate or when the rate constant for the decomposition of *BS* is slow.

Acknowledgement

H. Le gratefully acknowledges the Great Britain-China Educational Trust for its financial support.

References

[1] C. Mateo, J.M. Palomo, G. Fernandez-Lorente, J.M. Guisan, R. Fernandez-Lafuente, *Enzyme Microb. Tech.*, 2007, **40**,1451-1463.

[2] R.A. Sheldon, *Adv. Synth. Catal.*, 2007, **349**, 1289-1307.

[3] Y, Zhang, J. Ge, Z. Liu, *ACS Catal.*, 2015, **5**, 4503-4513.

[4] H. Bi, L. Qiao, J. Busnel, B. Liu, H.H. Girault, *J. Proteome Res.*, 2009, **8**, 4685-4692.

[5] Q. Li, X. Tu, J. Ye, Z. Bie, X. Bi, Z. Liu, *Chem. Sci.*, 2014, **5**, 4065-4069.

[6] C.O. Ania, A. Gomis-Berenguer, J. Dentzer, C. Vix-Guterl, *J. Electroanal. Chem.*, 2018, 808, 372-379.

[7] C.F. Megarity, B. Siritanaratkul, R.S. Heath, L. Wan, G. Morello, S.R. FitzPatrick, R.L. Booth, A.J. Sills, A.W. Robertson, J.H. Warner, N.J. Turner, F.A. Armstrong, *Angew. Chem. Int. Ed.*, 2019, **58**, 4948-4952.

[8] C. Wang, Z. Sheng, J. Ouyang, J. Xu, H. Chen, X. Xia, *ChemPhysChem*, 2012, **13**, 762-768.

[9] C. Wang, D. Ye, Y. Wang, T. Lu, X. Xia, *Lab Chip*, 2013, **13**, 1546-1553.

[10] H. Dai, Y. Li, Y. Fu, Y. Li, *Electroanal.*, 2018, **30**, 328-335.

[11] M. Roushan, Z. Azad, S. Movahed, P.D. Ray, G.I. Livshits, S.F. Lim, K.R. Weninger, R. Riehn, *Sci. Rep.*, 2018, **8**, 10036.

[12] C.F. Megarity, B. Siritanaratkul, B. Cheng, G. Morello, L. Wan, A.J. Sills, R.S. Heath, N.J. Turner, F.A. Armstrong, *ChemCatChem*, 2019, **11**, 5662-5670.

[13] L. Wan, R.S. Heath, B. Siritanaratkul, C.F. Megarity, A.J. Sills, M.P. Thompson, N.J. Turner, F.A. Armstrong, *Green Chem.*, 2019, **21**, 4958-4963.

[14] J.D. Gwyer, J. Zhang, J.N. Butt, J. Ulstrup, *Biophys. J.* 2006, **91**, 3897 –3906.

[15] J. Zhang, Q. Chi, A.G. Hansen, P.S. Jensen, P. Salvatore, J. Ulstrup, *FEBS Lett.* 2012, **586**, 526– 535.

[16] J.J. Davis, D. Djuricic, K.K.W. Lo, E.N.K. Wallace, L. Wong and H.A.O. Hill, *Faraday Discuss*., 2000,**116**, 15-22.

[17] I. Willner, M. Lion-Dagan, S. Marx-Tibbon and E. Katz, *J. Am. Chem. Soc.*, 1995, **117**, 6581-6592.

[18] I. Willner and B. Willner, *Bioelectrochem. Bioenerg*., 1997, **42**, 43-57.

[19] M.E.G. Lyons, *Sensors*, 2006, **6**, 1765-1790.

[20] M.E.G. Lyons, *Int. J. Electrochem. Sci.*, 2009, **4**, 77-103.

[21] M.E.G. Lyons, *Int. J. Electrochem. Sci.*, 2009, **4**, 1196-1236.

[22] P.N. Bartlett, K.F.E. Pratt, *Biosens. Bioelectron.*, 1993, **8**, 451-462.

[23] V. Flexer, K.F.E. Pratt, F. Garay, P.N. Bartlett, E.J. Calvo, *J. Electroanal. Chem.*, 2008, **616**, 87-98.

[24] V. Flexer, E.J. Calvo, P.N. Bartlett, *J. Electroanal. Chem.*, 2010, **646**, 24-32.

[25] L. Michaelis, M.L. Menten, *Biochem. Z.*, 1913, **49**, 333-369.

[26] K.A. Johnson, R.S. Goody, *Biochem.*, 2011, **50**, 8264-8269.

[27] R De Levie, *Adv. Electrochem. Electrochem. Eng.*, 1967, **6**, 329-397.

[28] S. Kondrat, A. Kornyshev, *J. Phys.: Condens. Matter*, 2013, **25**, 119501.

[29] C. Rochestera, A. Sartora, G. Pruessnerc, and A.A. Kornyshev, *Russ. J. Electrochem.*, 2017, **53**, 1165–1170.

[30] L. Becucci, R. Guidelli, *Langmuir*, 2007, **23**, 5601-5608.

[31] R. Guidelli, L. Becucci, *J. Solid State Electrochem.*, 2011, **15**, 1459–1470.

[32] R.G. Compton and C.E. Banks, *Understanding Voltammetry* (3nd Edition), London, World Scientific Press, **2018**.

[33] I.B. Svir, A.I. Oleinick, R.G. Compton, *Russ. J. Electrochem.* 2003, **39**, 160–164.

[34] R.G. Compton, E. Laborda, E. Kätelhön, K.R. Ward, *Understanding Voltammetry: Simulation of Electrode Processes* (2nd Edition), World Scientific Press, **2020**.

[35] M.P. Soriaga, A.T. Hubbard, *J. Am. Chem. Soc.*, 1982, **104**, 2742-2747.

[36] I. Streeter, G.G. Wildgoose, L. Shao, R.G. Compton, *Sens. Act. B*, 2008, **113**, 462-466.

[37] D. Peaceman, H. Rachford, Jr., *J. Soc. Ind. Appl. Math.*, 1955, **3**, 28–41.

[38] J. Heinze, *J. Electroanal. Chem. Interf. Electrochem.*, 1981, **124**, 73–86.

[39] J.A. Alden, R.G. Compton, *J. Phys. Chem. B*, 1997, **101**, 8941–8954.

[40] E. Kätelhön, R.G. Compton, *Analyst*, 2015, **140**, 2592–2598.

[41] E. Kätelhön, R.G. Compton, *Analyst*, 2015, **140**, 3290–3290.

[42] E. Kätelhön, R.G. Compton, *Analyst*, 2016, **141**, 1154–1154.

[43] C. Amatore, In *Physical Electrochemistry: Principles, Methods and Applications*; I. Rubinstein, Ed.; Marcel Dekker: New York, **1995**; Chapter 4.

[44] R.S. Tyurin, Y.S. Lyalikov, S.I. Zhdanov, *Russ. Chem. Rev.*, 1972, **41**, 1086-1100.

[45] E. Laviron, *J. Electroanal. Chem.*, 1979, **100**, 263-270.

[46] J. E. B. Randles, *Trans. Faraday Soc.*, 1948, **44**, 327–338.

[47] A. Ševcík, *Collect. Czech. Chem. Commun.*, 1948, **13**, 349–377.

[48] H. Chen, A.K.S. Kumar, H. Le, R.G. Compton, *J. Electroanal. Chem.*, 2020, **876**, 114730.

[49] H. Chen, R.G. Compton, *J. Electroanal. Chem.*, 2021, **880**, 114942.

[50] H. Chen, J. Elliott, H. Le, M. Yang, R.G. Compton, *J. Electroanal. Chem.*, 2020, **869**, 114185.